# Electric Potential of Citrate Capped Gold Nanoparticles is Affected by Poly(Allylamine Hydrochloride) and Salt Concentration

Xingfei Wei,† Alexander Popov,† and Rigoberto Hernandez*,†,‡,¶

†*Department of Chemistry, Johns Hopkins University, Baltimore, Maryland 21218, USA*

‡*Department of Chemical & Biomolecular Engineering, Johns Hopkins University, Baltimore, Maryland 21218, USA*

¶*Department of Materials Science and Engineering, Johns Hopkins University, Baltimore, Maryland 21218, USA*

E-mail: r.hernandez@jhu.edu

**Abstract**

The structure near polyelectrolyte-coated gold nanoparticles (AuNPs) is of significant interest because of the increased use of AuNPs in technological applications and the possibility that acquisition of polyelectrolytes can lead to novel chemistry in downstream environments. We use all-atom molecular dynamics (MD) simulations to reveal the electric potential around citrate capped gold nanoparticles (cit-AuNPs) and poly(allylamine hydrochloride) (PAH) wrapped cit-AuNP (PAH-AuNP). The ionic number distributions for both cit-AuNP and PAH-AuNP are calculated using MD simulations at varying salt concentrations (0 M, 0.001 M, 0.005 M, 0.01 M, 0.05 M, 0.1 M and 0.2 M NaCl). The net charge distribution ($Z(r)$) around the nanoparticle is determined from the ionic number distribution observed in the simulations, and allows for the calculation of the electric potential ($\phi(r)$). We find that the magnitude of $\phi(r)$

decreases with increasing salt concentration and upon wrapping by PAH. Using the consensus hydrodynamic radius ($R_{\mathrm{H}}$) from the literature and fits to the Debye-Hückel expression, we found and report the $\zeta$-potential for both cit-AuNP and PAH-AuNP at varying salt concentrations. For example, at 0.001 M NaCl, MD simulations suggest that $\zeta = -25.5$ mV for cit-AuNP. Upon wrapping of cit-AuNP by one PAH chain, the resulting PAH-AuNP exhibits a reduced $\zeta$-potential ($\zeta = -8.6$ mV). We also compare our MD simulation results for $\phi(r)$ to the classic Poisson-Boltzmann Equation (PBE) approximation and the well-known Derjaguin-Landau-Verwey-Overbeek (DLVO) theory. We find agreement with the limiting regimes—with respect to surface charge, salt concentration and particle size—in which the assumptions of the PBE and DLVO theory are known to be satisfied.

## Keywords

citrate capped gold nanoparticle, poly(allylamine hydrochloride), zeta-potential, hydrodynamic diameter, Poisson-Boltzmann Equation, DLVO theory

## 1 Introduction

Due to their unique physical and chemical properties, gold nanoparticles (AuNPs) have important applications in many materials areas, such as in sensing,[1] biomedicine,[2,3] and autonomous computing materials.[4,5] They can be easily synthesized through the the Turkevich method[6,7] in a sodium citrate and $HAuCl_4$ solution in which citrate ions act as both the reducing agent and the stabilizing ligand. The surface chemistry and structure of citrate molecules binding to AuNP surface has previously been extensively interrogated through scanning tunneling microscope (STM),[8] infrared spectroscopy (IR),[9,10] X-ray photoelectron spectroscopy (XPS),[9,10] nuclear magnetic resonance (NMR),[11] density functional theory (DFT) calculations[9,11,12] and molecular dynamics (MD) simulations.[13–15] The binding

energy between a citrate molecule and the Au surface was determined to be between 10-20 kcal/mol by both STM experiments and DFT methods.[8,11,12] The bond strength of the Au-O bond (for the O on -COOH) was also reported to be ∼2 kcal/mol which is lower than the Au-S bond.[8,10] The citrate surface concentration was also measured by Shumaker-Parry and coworkers[9,10] using XPS, and reported to be ∼1.7 molecules/nm$^2$ corresponding to a 45% coverage of the AuNP surface. MD simulations have also been used to uncover the atomistic structure of citrate molecules on the AuNP surface,[13,15] where most of the citrate molecules were found to have between 1 and 2 -COOH groups bonded to the surface Au atoms.

The nano-bio interfacial interaction is directly related to the toxicity of nanoparticles, and thereby also critically important in developing design rules for sustainable nanotechnologies.[16–21] Non-toxic citrate capped AuNPs (cit-AuNPs) can be functionalized through wrapping by poly(allylamine hydrochloride)s (PAHs), and thereby become toxic. It was reported that due to the strong interactions between the positively charged PAH wrapped cit-AuNP (PAH-AuNP) surface and the negatively charged bacterial surface, the PAH-AuNPs are toxic to two types of environmentally beneficial bacteria, namely *Shewanella oneidensis* and *Bacillus subtilis*.[17] PAH-AuNPs have also been seen to be increasingly toxic to Gram-negative bacteria whose membranes consist of increasingly smooth lipopolysaccharides (LPS).[21] Through the use of MD simulations, this trend was rationalized as being a consequence of the greater number of PAH binding sites in smooth LPS relative to rough LPS.[21]

The nanoparticle surface charge density and surface potential of AuNPs have been seen to play a crucial role at the nano-bio interface.[22–26] The AuNP surface charge can be tuned from negative to positive through the use of a layer-by-layer wrapping construction, in which a nanoparticle is wrapped in alternating layers of cationic and anionic polyelectrolytes.[22,23] Both experimental and simulation results have shown that cationic (16-mercaptohexadecyl)trimethylammonium bromide coated AuNPs (MTAB-AuNPs) bind to

$\alpha$-Synuclein proteins more strongly than anionic cit-AuNPs.[24] Experiments have also found that hydrogen-bonding interactions induce strong binding of cationic PAH-AuNPs to $\alpha$-Synuclein protein and even lead to aggregation.[24] Thus AuNP surface charge is directly related to the strength of nano-bio interfacial interactions.

The salt concentration effect on nano-bio interfacial interaction is another important issue. Geiger and coworkers[25,26] found that at 0.1 M NaCl concentration, both anionic 3-mercaptopropionic acid coated AuNPs (MPA-AuNPs) and cationic PAH-AuNPs can attach to a negatively charged lipid bilayer. Their results suggest that the binding of anionic MPA-AuNPs and cationic PAH-AuNPs with the same lipid bilayer result from two entirely different mechanisms. Nevertheles, NaCl ions play a critical role to the binding interaction in both cases.[25] Unfortuantely, the fundamental physics and chemistry of the ionic concentration effect on nano-bio interfacial interaction remains unclear, and this work aims to provide some answers in this direction.

One approach to interrogating the elctric potential of AuNPs relies on the known correlation between the electric potential and electric double layer (EDL) near the surface of a colloidal particle and their colloidal properties.[27] For example, it was reported that cit-AuNPs can remain stable when in contact with $\alpha$-Synuclein proteins, but PAH-AuNPs will form aggregates.[24] In general, the $\zeta$-potential of the particle can be used to interpret the resulting colloidal stability: if $|\zeta| < 10$ mV, the colloid is likely to be highly unstable, whereas if $|\zeta| > 30$ mV, the colloid is likely to be highly stable.[27] Even though the colloidal stability is easily observable in experiments, $\zeta$-potential measurements have high uncertainty, and they are the highest for small nanoparticles. To our knowlege, there exist three primary references that have reported the measurement of the $\zeta$-potential for cit-AuNP: Rostek *et al.*[28] reported $\zeta \sim -35$ mV, Dominguez *et al.*[29] reported $\zeta \sim -15$ mV and Lin *et al.*[24] reported $\zeta \sim -13$ mV. However, these cit-AuNPs are not the same materials which explains in part why the values are so different. Dominguez *et al.*[29] estimated the core diameter of their particles to be 4.9 nm in 0.001 M, Lin *et al.*[24] estimated the core diameter to be 12 nm

in 0.02 M 4-(2-hydroxyethyl)-1-piperazineethanesulfonic acid (HEPES), and Rostek *et al.*[28] did not explicitly report the core diameter or salt concentration—but one might infer that they found it to be roughly $\sim$ 20 nm and 0.001-0.01 M NaCl. MPA-AuNP is comparable to that for cit-AuNP, and there exist at least two reported values of the $\zeta$-potential: Feng *et al.*[17] reported $\zeta \sim -36$ mV and Troiano *et al.*[25] reported $\zeta \sim -29$ mV. They found agreement in the $\zeta$-potential for MPA-AuNPs with core diameter 4.2 nm in 0.001 M NaCl. However, the salt concentration effect on the $\zeta$-potential and stability of the MPA-AuNP remains unclear. In 0.001 M NaCl, Troiano *et al.*[25] found that the hydrodynamic diameter ($D_{\mathrm{H}}$) of MPA-AuNP is $\sim$ 9 nm with $\zeta \sim -29$ mV, but in 0.1 M NaCl, due to aggregation, $D_{\mathrm{H}}$ increased to 100-400 nm for $\zeta \sim -27$ mV. It is unclear why the $\zeta$-potential only changed by 2 mV in 0.1 M NaCl , but the MPA-AuNP appeared to be highly unstable. Meanwhile, Troiano *et al.*[25] also measured that in 0.001 M NaCl $D_{\mathrm{H}}$ of PAH-AuNP was only $\sim$ 6 nm $\zeta \sim +38$ mV, and in 0.1 M NaCl due to aggregation $D_{\mathrm{H}}$ of PAH-AuNP increased to 20-80 nm $\zeta \sim +32$ mV. It is also curious that the PAH-AuNPs showed different stabilities in 0.1 M NaCl, but the $\zeta$-potentials are very similar and $\zeta > +30$ mV in the highly stable region.[25,26] Due to wrapping by PAH, the properties of the ion distribution and electrical potential near the PAH-AuNP are more complex than that for the cit-AuNP. For the PAH-AuNP with $\sim$ 4.5 nm diameter core size at low salt concentration region, the $\zeta$-potential was typically reported between +30 and +40 mV, but $D_{\mathrm{H}}$ varies a lot, for example, Troiano *et al.*[25] reported $\zeta \sim +38$ mV with $D_{\mathrm{H}} \sim 6$ nm in 0.001 M NaCl, Feng *et al.*[17] reported $\zeta \sim +38$ mV ($D_{\mathrm{H}}$ not available) in 0.001 M NaCl, and Buchman *et al.*[21] reported $\zeta \sim +34$ mV with $D_{\mathrm{H}} \sim 12$ nm in 0.025 M NaCl. Meanwhile, Qiu *et al.*[20] reported $\zeta \sim +66$ mV with $D_{\mathrm{H}} \sim 38$ nm, for the same PAH-AuNP $\sim$ 4.5 nm diameter core in 0.001 M NaCl, which was due to additional unbonded PAHs inside the colloid. However, some research groups reported much lower $\zeta$, which requires further verification, for example, Dominguez*et al.*[29] reported $\zeta \sim +18$ mV with $D_{\mathrm{H}} \sim 18$ nm at a core diameter 4.7 nm, and Han *et al.*[30] even reported $\zeta \sim -35$ mV (a negtive value) with $D_{\mathrm{H}} \sim 74$ nm at a core diameter 21 nm. The $\zeta$-potential and EDL of

both cit-AuNP and PAH-AuNP are still unsolved, especially at different salt concentrations. An atomistic understanding about the surface charge, ion distribution and $\zeta$-potential of these two colliods, as pursued in this work, could help resolve the many outstanding questions concerning the effects of the electric potential and the ensuing interaction properties of AuNPs.

Computational methods have played an important role in revealing the fundamental mechanism of nanoparticle interactions with bio-membranes at different scales.[19,31] Previously, our group used all-atom (AA) and coarse-grained (CG) MD simulation models to uncover the structure of citrate molecules on the cit-AuNP, and the conformation of a PAH chain wrapping around a cit-AuNP.[15,32] In this work, the salt concentration and PAH wrapping effects on the electric potential of the cit-AuNP are revealed using AA-MD of these model systems solvated by implicit water. First, the radial distributions of the ion number density are calculated at different NaCl concentrations (0-0.2 M), are are used to obtain charge density radial distributiosns. Then, the electric field is calculated from the charge distribution. The electric potential is calculated by integrating the electric field that satisfies the corresponding boundary conditions (BCs). We find that the electric potential changes after wrapping by a PAH chain, and is affected by the NaCl concentration. The $\zeta$-potential is determined from the electric potential at the hydrodynamic radius ($R_{\mathrm{H}} = D_{\mathrm{H}}/2$). Using MD simulations, we confirm that wrapping by PAH can reduce the magnitude of the $\zeta$-potential of a AuNP and its colloidal stability. Our MD simulation results for the electric potential compares well with the appropriatel limits of the classic Poisson-Boltzmann Equation (PBE) approximation and the Derjaguin-Landau-Verwey-Overbeek (DLVO) theory.

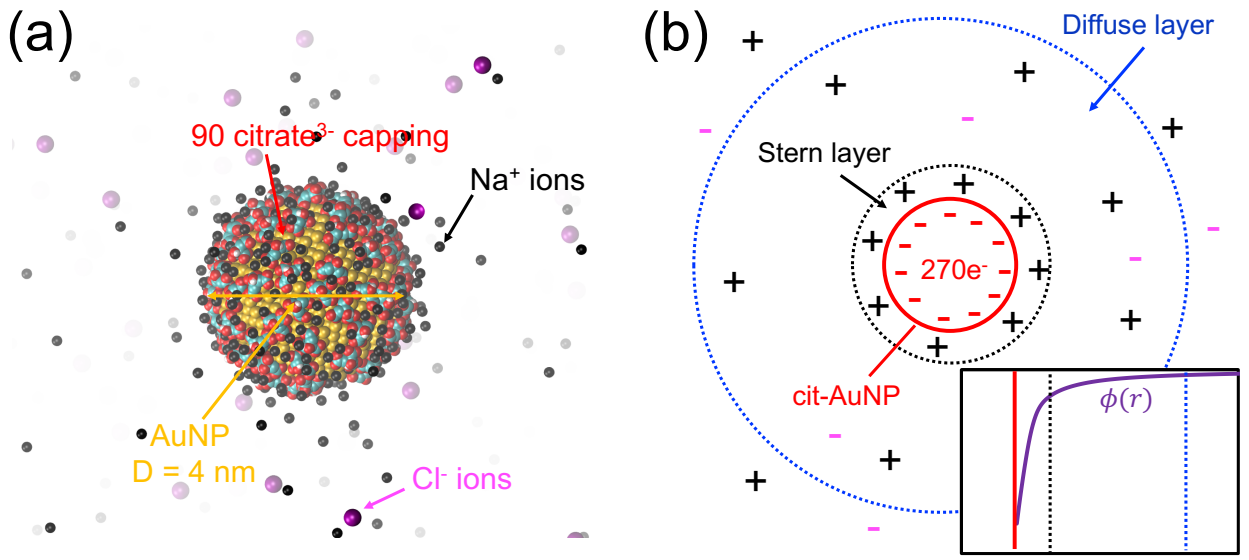


Figure 1: (a) The MD simulation model of the cit-AuNP surrounded with $Na^+$ and $Cl^-$ ions. (b) The electric double layer scheme of the cit-AuNP model, where the solid red line indicates the AuNP surface, the black dotted line indicates the outer edge of the Stern layer, and the blue dotted line indicates the outer edge of the diffuse layer. The inset indicates the form of the electric potential $\phi$ from the center of the AuNP with the corresponding edges marked accordingly.

# 2 Methods

## 2.1 MD simulations

*Simulation models.* The cit-AuNP model shown in Fig. 1a includes a 4 nm diameter AuNP core in the center, 90 $Citrate^{3-}$ molecules bonded the AuNP surfaces, and $Na^+$ and $Cl^-$ ions, all in an implicit solvent. At this surface coverage, the citrate concentration is 1.79 molecule/$nm^2$ and the surface charge density is $8.93 \times 10^{-10}$ mol/$cm^2$ ($-5.4$ $e$/$nm^2$). These values for the citrate and charge density are comparable to experimental measurements[9,10,33,34] and previous simulation models.[15,32,35] We simulated 12 different systems, including 6 NaCl concentrations (0 M, 0.001 M, 0.005 M, 0.01 M, 0.05 M, 0.1 M and 0.2 M) for both cit-AuNP and PAH-AuNP models. The cit-AuNP carries $Q = -270$ $e$ surface charges. Consequently, even at 0 M NaCl, counterions must be added to neutralize the net charge. Specifically, 270 $Na^+$ counterions are added to the saltless case, leading to an ionic strength of

0.0002 M. The overall NaCl concentration ($c_{\mathrm{Na^+}}$ and $c_{\mathrm{Cl^-}}$) is calculated by dividing the total number of NaCl pairs by the volume of the simulation box. The bulk concentrations ($c^{\infty}_{\mathrm{Na^+}}$ and $c^{\infty}_{\mathrm{Cl^-}}$) are taken to be the ion concentrations far away from the cit-AuNP, and differ from the overall concentration because the ions form a Stern layer on the cit-AuNP surface with a differing concentration. Table S1 in Supporting Information (SI) lists the exact number of $Na^+$ and $Cl^-$ ions in the simulation box, and their overall and bulk concentrations.

The simulation box size is 100×100×100 $nm^3$. The relative scale of the cit-AuNP at a concentration of 1.66 $\mu$M and the ion coverage within the simulation box can be found in Fig. S1 in SI. This AuNP concentration is larger than that used in typical experiments at circa 10 nM.[20,25] However, a smaller concentration would require an even larger simulation box, and the present choice is already at the limits of our computational resources. Nevertheless our results suggest that this is large enough to calculate a converged $R_{\mathrm{H}}$ and $\zeta$-potential for 4 nm core diameter cit-AuNPs and PAH-AuNPs. Figure 1b shows the ion radial distribution and electric potential scheme of cit-AuNP. The EDL structure forms near cit-AuNP, where the Stern layer directly attaches to the surface and the diffuse layer is just outside the Stern layer. The electric potential $\phi(r)$ scheme is also shown in the small panel in Fig. 1b. Similarly, Fig. S2 in SI shows the model and scheme of the PAH-AuNP, which has one PAH chain wrapped on the cit-AuNP.

*Simulation protocols.* All MD simulations in this paper are propagated using the Large-scale Atomic Molecular Massively Parallel Simulator (LAMMPS) package.[36] The pairwise force field parameters are listed in Tables S2 and S3 in SI. The Lennard-Jones (LJ) force field is used to describe the Au-Au interactions in the 4 nm diameter AuNP in an fcc crystal structure.[37] The PAH chain with 200 repeating units and the $Citrate^{3-}$ molecules are built using Moltemplate.[38,39] The Optimized Potentials for Liquid Simulations (OPLS)-AA force field is used to describe the interactions for $Citrate^{3-}$ and PAHs, and the hydrogen atoms bonded to carbons are lumped together using the OPLS-UA (united atom) force field.[15,32,40,41] The Au-citrate bonding interaction is simulated using a LJ force field, by setting the energy con-

stant between Au and oxygens (on the -$COO^-$) to 2 kcal/mol. This binding energy setting is consistent with those used in Refs. 8, 10 and 11. During our simulations, all citrates stay on the AuNP surface. Interactions between Au and other organic compounds are set according to Ref. 42; see Table S3 in SI for details. The cutoffs for LJ and Coulombic force are both set at 10 Å. The long-range Coulombic force is calculated using the Ewald summation method based on the particle-particle particle-mesh (PPPM) algorithm.[43–45] The dielectric constant is set to 80 as is typical for an implicit water model.[15,32,41]

Initially, the $Na^+$ and $Cl^-$ ions are uniformly and randomly distributed across the box by applying 600 K $NVT$ relaxation simulations to the ions for a few nanoseconds. More than 20 ns of relaxaxtion $NVT$ simulations ($T = 300$ K, Langevin thermostat) are applied to further achieve an equilibrium ionic distribution. We also found that this convereged the average number of $Na^+$ and $Cl^-$ ions within the diffuse and Stern layers. For example, the convergence of $Na^+$ cations within a 50 Å shell from the AuNP center for the 0.001 M, 0.01 M and 0.1 M NaCl models can be found in Fig. S3 in SI. After the system reaches equilibrium, we propoagate more than 10 $NVT$ ensembles using the Langevin thermostat at 300 K to collect the $Na^+$ and $Cl^-$ distributions. The simulation damping parameter is 100 fs, the timestep is 1 fs, the typical simulation time is 1 ns, and a different random seed is used for each run. The trajectory is recorded every 10,000 timesteps. Production runs of 10-20 ns simulation time are used to sample enough independent structures along the trajectories (1000-2000 frames) to obtain converged ionic distributions. The corresponding histograms are obtained for the ion concentrations with bins of size 0.5 Å.

## 2.2 Theory

*MD simulation method.* The electric potential can be found via the integration of the electric field:[46]

$$\phi(r) = -\int_{R_0}^{r} \frac{Z(x)}{4\pi\epsilon x^2} dx + C\,, \tag{1}$$

where $R_0 = 20$ Å is the nanoparticle radius, and $\varepsilon = 80 \times \varepsilon_0$ is the dielectric permitivity of the solvent environment (vacuum permitivity $\varepsilon_0 = 8.85 \times 10^{-12}$ C/V/m). The constant $C$ is determined by the BC,[47,48]

$$\phi(r)|_{r=\infty} = 0\,. \tag{2}$$

The total charge contained within the sphere of radius $r$ is

$$Z(r) = Q + \int_{R_0}^{r} 4\pi x^2 \rho(x) dx\,. \tag{3}$$

The net surface charge $Q$ at $r = R_0$ is $-270\ e$ for cit-AuNP and $-70\ e$ for PAH-AuNP. The charge density $\rho(r)$ is calculated from the ionic concentrations $c_{\mathrm{Na^+}}(r)$ and $c_{\mathrm{Cl^-}}(r)$ as

$$\rho(r) = eN_{\mathrm{A}}\left[c_{\mathrm{Na^+}}(r) - c_{\mathrm{Cl^-}}(r)\right]\,, \tag{4}$$

where $e = 1.60 \times 10^{-19}$ C and $N_{\mathrm{A}} = 6.022 \times 10^{23}$.

Numerical integration of $\phi(r)$ as per Eq. (1) is performed using the trapezoidal rule on a mesh of size $h = 0.5$ Å. Since we can not accurately obtain the potential at $r = \infty$, we cut off the integral at $r = 800$ Å where $\phi \approx 0$. This assumption is justified by noticing that the average difference of $\phi$ values at $r = 500$ Å and $r = 800$ Å constitute an insignificant contribution of about 0.4 mV; see Figs. S5 and S11 in SI.

*The PBE approximation.* In spherical coordinates, the electric potential $\phi(r)$ is related to the charge density $\rho(r)$ through the Poisson equation:[47–50]

$$\nabla^2\phi(r) = \frac{2}{r}\frac{d\phi(r)}{dr} + \frac{d^2\phi(r)}{dr^2} = \frac{-\rho(r)}{\varepsilon}\,. \tag{5}$$

The charge density $\rho(r)$ is calculated from the ionic concentrations $c_{\mathrm{Na^+}}(r)$ and $c_{\mathrm{Cl^-}}(r)$ as

$$\rho(r) = eN_{\mathrm{A}}\sum_{i=1}^{m} z_i c_i(r)\,, \tag{6}$$

where $z_i$ is the partial charge of ion type $i$, and $m$ is the total number of different types of ions. The PBE theory is based on the assumption that the ion concentrations in Eq. (4) follows Boltzmann statistics:

$$c_i(r) = c_i^{\infty} \exp\left[\frac{-z_i e\phi(r)}{k_{\mathrm{B}}T}\right], \tag{7}$$

where $k_{\mathrm{B}} = 1.38 \times 10^{-23}$ J/K the $T = 300$ K. The superscript in the concentrations $c_i^{\infty}$ for $Na^+$ and $Cl^-$ refer to the bulk limit. Using MD trajectories, $c_i^{\infty}$ are computed from the solvent region found between $r = 300$ Å and $r = 500$ Å away from the nanoparticle (see Figs. S4 and S10 in SI). Combining Eqs. (5) and (7), the PBE equation can be written as:

$$\nabla^2\phi(r) = \frac{-eN_{\mathrm{A}}}{\varepsilon} \sum_{i=1}^{m} z_i c_i^{\infty} \exp\left[\frac{-z_i e\phi(r)}{k_{\mathrm{B}}T}\right], \tag{8}$$

which is solved by the finite difference scheme:

$$\begin{aligned} &\frac{2}{r_k}\frac{\phi(r_{k+1}) - \phi(r_{k-1})}{2h} + \frac{\phi(r_{k+1}) - 2\phi(r_k) + \phi(r_{k-1})}{h^2} \\ &= \frac{-eN_{\mathrm{A}}}{\varepsilon}\left(c_{\mathrm{Na^+}}^{\infty} \exp\left[\frac{-e\phi(r_k)}{k_{\mathrm{B}}T}\right] - c_{\mathrm{Cl^-}}^{\infty} \exp\left[\frac{e\phi(r_k)}{k_{\mathrm{B}}T}\right]\right). \end{aligned} \tag{9}$$

The electric potential is solved using standard Matlab code, applying two BCs:

$$\phi(r)\big|_{r=a_i} = \frac{Z(a_i)}{4\pi a_i \varepsilon}, \tag{10}$$

$$\left.\frac{d\phi(r)}{dr}\right|_{r=a_i} = \frac{Z(a_i)}{4\pi a_i^2 \varepsilon}, \tag{11}$$

where the ionic shell at $r = a_i$ is related to the Stern layer, and $Z(a_i)$ is the total net charge inside the ionic shell. At different NaCl concentrations, we use the same $a_i = 35$ Å for the cit-AuNP model, and we varied $a_i$ for the PAH-AuNP models. All parameters used to solve the PBE approximation, including $a_i$ and $Z(a_i)$, are listed in Table S4 in SI.

*The DLVO theory.* The well-known DLVO theory[51] has been successfully applied to

estimate colloid-colloid interaction potentials throughout the literature.[52–56] The DLVO potential can be written as:[52–54]

$$V_{\mathrm{DLVO}}(r) = \frac{Q^2}{\varepsilon r}\frac{\exp[-(r-2R)/\lambda_{\mathrm{D}}]}{(1+R/\lambda_{\mathrm{D}})^2}\,,\ r > 2R\,, \tag{12}$$

where $Q$ is the colloidal charge, $R$ is the radius of the colloidal particle, and $\lambda_{\mathrm{D}}$ is the Debye screening length,

$$\lambda_{\mathrm{D}} = \sqrt{\frac{\varepsilon k_{\mathrm{B}} T}{e^2 N_A \sum_{i=1}^{m} z_i^2 c_i}}\,. \tag{13}$$

Here we use the same $Q = Z(a_i)$ and $R = a_i$ as in the PBE approximation. The electric potential of a single colloid is written as:[51]

$$\phi_{\mathrm{DLVO}}(r) = \frac{Q}{\varepsilon r}\frac{\exp[-(r-R)/\lambda_{\mathrm{D}}]}{1+R/\lambda_{\mathrm{D}}}\,,\ r > R. \tag{14}$$

Parameters used to solve Eq. (14) are listed in Table S4 in SI. For convenience, $\lambda_{\mathrm{D}}$ is calculated here according to the overall salt concentrations ($c_{\mathrm{Na^+}}$ and $c_{\mathrm{Cl^-}}$). Table S4 in SI confirms that $\lambda_{\mathrm{D}}$ values are very close to $\lambda_{\mathrm{D}}^{\infty}$ when the salts are at their bulk concentrations ($c_{\mathrm{Na^+}}^{\infty}$ and $c_{\mathrm{Cl^-}}^{\infty}$), except in low salt conditions ($< 0.001$ M). As a result, use of the approximation, $\lambda_{\mathrm{D}} \approx \lambda_{\mathrm{D}}^{\infty}$, does not significantly affect our results or discussion.

# 3 Results and discussion

## 3.1 The ion radial distributions and electric potential near cit-AuNP

*Ion radial distributions near cit-AuNP.* The radial ion distributions near cit-AuNP are shown in Fig. 2. The AuNP core radius is highlighted with a solid vertical line at 20 Å. The citrates in the capping layer are located at 20-23.5 Å, and the Stern layer is highlighted with a dashed vertical line at 35 Å. At different salt concentrations, we found that the $Na^+$ peaks always appear at $\sim$ 27 Å. After 35 Å, the curves decrease smoothly and monotonically; see Fig. 2a.

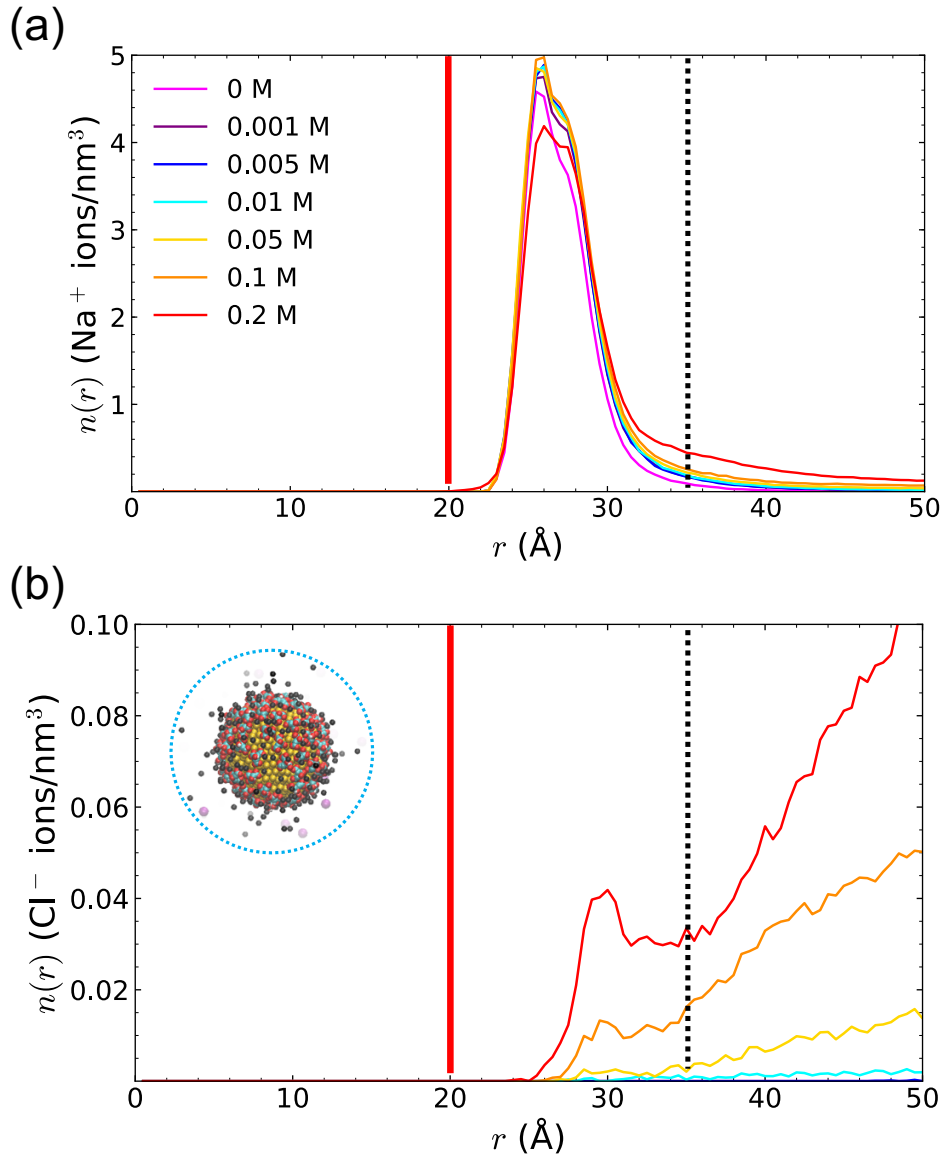


Figure 2: The number densities radial distribution of $Na^+$ and $Cl^-$ for the cit-AuNP model at different NaCl concentrations —with molarities indicated in the legend of panel a— are shown in (a) and (b), respectively. The solid red line at 20 Å indicates the AuNP surface and the black dotted line at 35 Å indicates the outer edge of the Stern layer. The ion number densities beyond radius 50 Å are available in Fig. S4 of the SI.

On the other hand, according to Fig. 2b, we find that the $Cl^-$ number densities generally increase smoothly beyond 35 Å. At high salt concentrations (0.1 M and 0.2 M), we also find in Fig. 2b that the $Cl^-$ number densities exhibit small peaks at $\sim 30$ Å, which is accordingly a consequence of the ion-ion interactions.

In this work, we focus on the low concentration range 0.001-0.1 M, which is near the typical salt concentration, 0.01 M, of biological cells. At high salt concentrations, the ion-ion interaction effect becomes significant, and addressing it is beyond the scope of the present work. We refer to the starting model as having a 0 M NaCl concentration—which is technically correct—even though it requires countercharges in order to maintain charge neutrality; namely it contains 270 $Na^+$ (and no $Cl^-$) in our simulation box. Figure S4 in SI shows that the $Na^+$ and $Cl^-$ number densities approach the bulk concentrations after 200 Å. The averages of the ions concentrations in the 300-500 Å region are used to obtain the bulk number densities and bulk concentrations ($c^{\infty}_{Na^+}$ and $c^{\infty}_{Cl^-}$).

*Electric potential near the cit-AuNP.* The total net charge $Z(r)$ inside $r$ is calculated from the ionic distribution in Fig. S5a in SI. We found that the net charge $Z(r)$ converges to 0—viz charge neutral—inside $r < 300$ Å at all concentrations except in the 0 M NaCl model. This suggests that the simulation box is sufficiently large $r = 500$ Å to obtain these electric potentials and other properties. In what follows, we focus on the concentration region of interest between 0.001 and 0.1 M NaCl, and do not discuss results for two limiting regimes, 0 M and 0.2 M NaCl. These limiting cases, however, are not necessarily in the same thermodynamic regime because in the case of 0 M NaCl we have no $Cl^-$ ions in the bulk, and in the case of 0.2 M NaCl the concentrations are so large that effects of ion-ion pairing become important.

The electric potential $\phi(r)$ solved using Eq. (1) for total net charge $Z(r)$ is shown in Figure S5b in SI. Figure 3a shows a zoomed-in picture of $\phi(r)$, where they are also compared to experimental results of the $\zeta$-potential and $R_H$. One important observation from Fig. 3a is that the magnitude of the electric potential decreases with increasing salt concentration

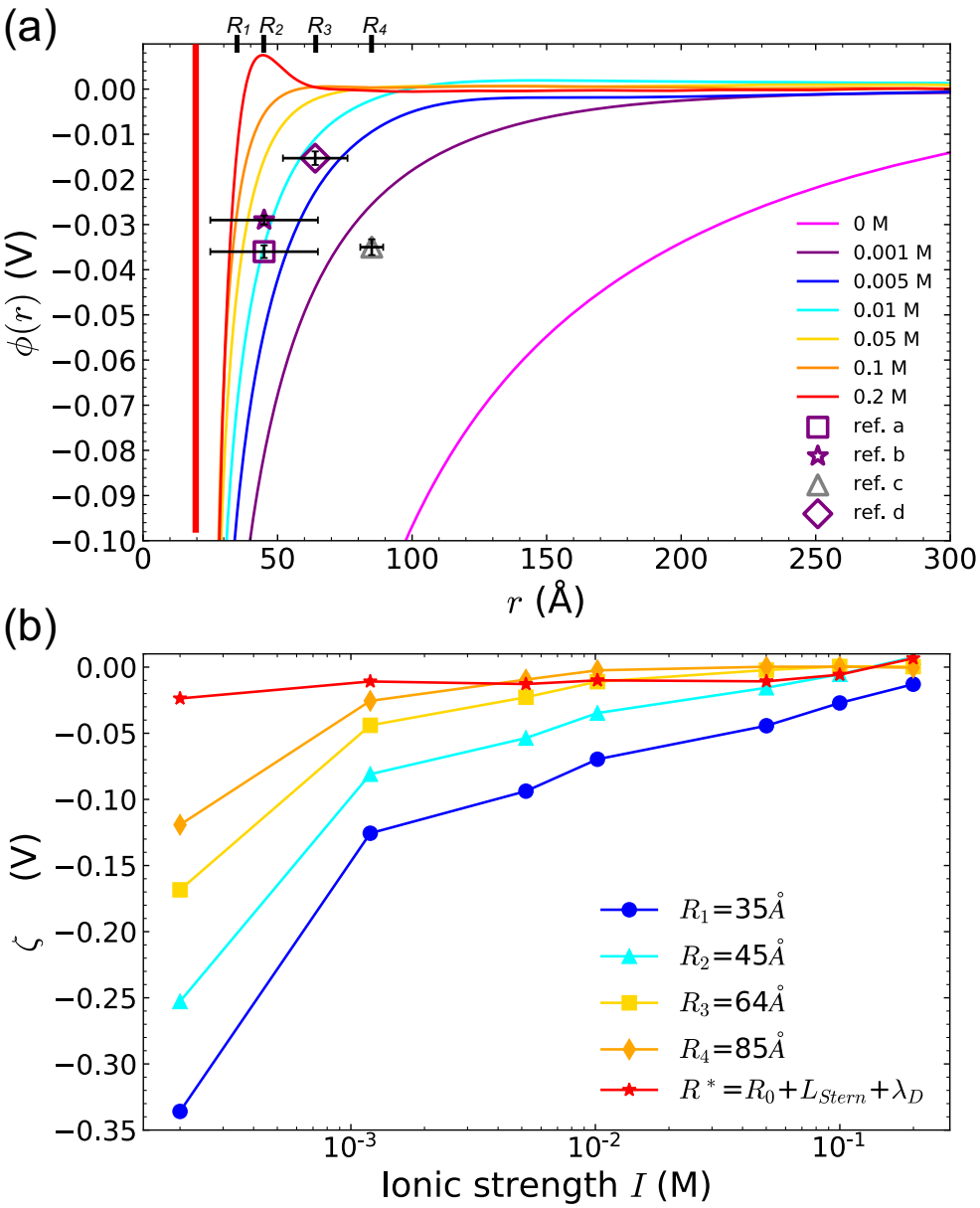


Figure 3: (a) Comparison between the electric potential near cit-AuNP between those observed in MD simulations at various NaCl concentrations, and those reported in literature. (b) Values of the cit-AuNP $\zeta$-potential, determined from the MD results in panel a, as a function of the solvent's ionic strength for different estimates of the nanoparticle's hydrodynamic radius $R_{\mathrm{H}}$. Here, $R_1 = 35$ Å is determined from the MD ion distribution results, $R_2 = 45$ Å is from ref. a (viz. Ref. 17) and ref. b (viz. Ref. 25) with MPA-AuNP in 0.001 M NaCl, $R_3 = 64$ Å is from ref. d (viz. Ref. 29) with cit-AuNP in 0.001 M NaCl, and $R_4 = 85$ Å is from ref. c (viz. Ref. 28) with cit-AuNP unknown salt concentration. Ref. 17 did not report $D_{\mathrm{H}}$ explicitly but they used the same type of MPA-AuNP particles as in Ref. 25, and hence we assign it to be the same corresponding value. As the uncertainty in the reported value of ref. c (viz. Ref. 28) was not reported, we have included an estimated error bar of 5% in the figure.

which indicates the cit-AuNP is less stable at high salt concentrations. The $\zeta$-potential values are determined from $\phi(r)$ at distances $R_{\rm H}$. Using a larger $R_{\rm H}$ distance, the magnitude of $\zeta$-potential decreases because $\phi(r)$ decays with $r$; see Fig. 3a. The hydrodynamic radius $R_{\rm H}$ (the slip layer position) can not be exactly determined in our implicit water MD simulation models. Instead, we use the experimental $R_{\rm H}$ values reported in the literature from dynamic light scattering (DLS) measurements, as cited below.

Table 1: Comparison of the $\zeta$-potential across cit-AuNPs of varying size and surface coverage between the literature and this work. Results references noted by footnotes *e-h* are plotted in Fig. 3a, and those from *i-l* are plotted in Fig. 6a.

| Ref. | Ligand | $\zeta$-potential (mV) | NaCl (M) | $D_0$ (nm)[a] | $D_{\rm H}$ (nm)[b] | Charge (e/nm$^2$) |
|---|---|---|---|---|---|---|
| [ 29][h] | Citrate | -15.3 ± 1.5 | 0.001 | 4.9 ± 1.4 | 12.8 ± 1.2 | N/A |
| [ 24] | Citrate | -13.44 ± 1.77 | 0.02 M HEPES | 12 | N/A | N/A |
| [ 28][g] | Citrate | ∼ -35 | N/A | N/A | 17 | N/A |
| this work | Citrate | -25.5 | 0.001 | 4 | 17 | -5.4 |
| this work | Citrate | -2.4 | 0.01 | 4 | 17 | -5.4 |
| this work | Citrate | +0.3 | 0.1 | 4 | 17 | -5.4 |
| [ 17][e] | MPA | -36.0 ± 1.4 | 0.001 | 4.2 ± 1.2 | N/A | -5.6 |
| [ 25][f] | MPA | -29 ± 1 | 0.001 | 4.2 ± 1.2 | 9 ± 2 | ∼-4.0 |
| [ 25] | MPA | -27 ± 2 | 0.1 | 4.2 ± 1.2 | 100-400 (Agg.[d]) | ∼-4.0 |
| [ 20][i] | PAH | +66 ± 2 | 0.001 | 4.5 ± 1.2 | 38 | N/A |
| [ 17] | PAH | +38.4 ± 1.8 | 0.001 | 4.7 ± 1.5 | B. L.[c] | +12.8 |
| [ 25][k] | PAH | +38 ± 3 | 0.001 | 4.5 ± 1.4 | 6 ± 2 | ∼-4.0 to +4.0 |
| [ 29][l] | PAH | +17.9 ± 0.9 | 0.001 | 4.7 ± 1.2 | 17.9 ± 0.9 | N/A |
| [ 21][j] | PAH | +34 ± 2 | 0.02 M HEPES | 4.2 ± 1.2 | 12 ± 2 | N/A |
| [ 57] | PAH | ∼ +48 | 0.01 | 20 | N/A | N/A |
| [ 25] | PAH | +32 ± 2 | 0.1 | 4.5 ± 1.4 | 20-80 (Agg.[d]) | ∼-4.0 to +4.0 |
| [ 26] | PAH | +32 ± 2 | 0.1 | 4.5 ± 1.4 | 129 ± 1 | -0.25 ± 0.5 |
| [ 26] | PAH | +24 ± 2 | 0.1 | 13.9 ± 2.6 | 137 ± 2 | N/A |
| [ 26] | PAH | +24 ± 2 | 0.1 | 13.9 ± 2.6 | 590 ± 2 (Agg.[d]) | N/A |
| [ 30] | PAH | ∼ -35 | 0.01 M HEPES | 21 | 74.2 | N/A |
| this work | one PAH | -8.6 | 0.001 | 4 | 17.9 | -1.4 |
| this work | one PAH | +0.2 | 0.01 | 4 | 17.9 | -1.4 |
| this work | one PAH | +0.2 | 0.1 | 4 | 17.9 | -1.4 |

[a] $D_0$ is the AuNP core diameter; [b] $D_{\rm H}$ is the hydrodynamic diameter; [c] B. L. refers to measurements beyond limitations; [d] Agg. refers to particles in an aggregate; [e] ref. a in Fig. 3a, [f] ref. b in Fig. 3a, [g] ref. c in Fig. 3a, [h] ref. d in Fig. 3a, [i] ref. a in Fig. 6a, [j] ref. b in Fig. 6a, [k] ref. c in Fig. 6a, [l] ref. d in Fig. 6a.

*$\zeta$-potential and $R_H$ calculations for the cit-AuNP.* The $\zeta$-potential and $D_{\rm H}$ values of cit-AuNP and MPA-AuNP, are compared in the first 9 rows in Table 1. The PAH-AuNP results, from the 10th row to the end of Table 1, will be discussed later. Four reference $\zeta$-potential values are plotted together with our MD electric potential $\phi(r)$ in Fig. 3a. It is notable that Refs. 17 and 25 used MPA-AuNPs with a core diameter 4.2 nm and a surface

charge density of $\sim -5.6\ e/\mathrm{nm}^2$ in $\sim 0.001$ M NaCl, which is close to our MD cit-AuNP model (4 nm AuNP, $\sim -5.4\ e/\mathrm{nm}^2$, $\sim 0.001$ M NaCl).

Several different $R_\mathrm{H}$ distances have been reported in the literature cited in Table 1, so we must compare $\zeta$-potentials using different radii ($R_1$, $R_2$, $R_3$, $R_4$ and $R^*$). Here, $R_1 = 35$ Å is obtained from the charge density (see Fig. S6a in SI and Fig. 2), and is related to the onset of the Stern layer. Meanwhile, $R_2 = 45$ Å, $R_3 = 64$ Å and $R_4 = 85$ Å were reported in Refs. 25, 29 and 28, respectively. The radius $R^*$ is calculated from the summation of AuNP core radius ($R_0$), Stern layer thickness ($L_\mathrm{Stern}$) and Debye length ($\lambda_\mathrm{D}$) ($R^* = R_0 + L_\mathrm{Stern} + \lambda_\mathrm{D}$, see Table S5 in SI), and includes the salt concentration effect on $R_\mathrm{H}$.

In MD simulations, the slipping boundary ($R_\mathrm{H}$) can also be estimated by fitting to the tail of the $Na^+$ radial distribution with the Debye-H*ü*ckel expression, $A^{-Br}/r + C$; the slipping boundary ($R_\mathrm{H}$) was previously identified as the location where the fit deviates from the data.[58] In the present work, we updated the form of the tail of the distribution using the PBE approximation resulting in $c{\cdot}\exp[-e\phi(r)/k_\mathrm{B}T]$, where $\phi(r)$ is calculated through Eq. (1). We find the deviation (slipping) happens at 40-70 Å for cit-AuNP, see Fig. S7a in SI, and our selected $R_1$, $R_2$, $R_3$, $R_4$ and $R^*$ have already included this region.

For fixed $R_\mathrm{H}$, the magnitude of $\zeta$ is seen in Figure 3b to monotonically decrease with increasing salt concentration. At $R_1 = 35$ Å, $R_2 = 45$ Å and $R_3 = 64$ Å in 0.001 M NaCl, we see that $\zeta \approx -125.6$, $-81.0$ and $-44.0$ mV, respectively, which are much larger in magnitude than reported in experiments. Meanwhile if we set $R^* = 123$ Å, we obtain $\zeta = -10.9$ mV in 0.001 M NaCl, which is too small. Therefore, we suppose that $R_4 = 85$ Å ($D_\mathrm{H} = 17\ nm$) is the best choice consistent with experiments; see Table 1. We also found that $\zeta = -25.5$ mV at $R_\mathrm{H} = 85$ Å (in 0.001 M NaCl), which lies inside the range of experimentally reported values of $-15.3$ mV in Ref. 29, $-36.0$ mV in Ref. 17 and $-29$ mV in Ref. 25. Our finding is consistent with Ref. 27, which provided the criteria for the stability of cit-AuNP in 0.001 M NaCl that the $\zeta$ potential be less negative than $-30$ mV. The smaller-in-magnitude value, $\zeta = -13.44$ mV, reported in Ref. 24 is consistent because the latter was measured at a higher

salt concentration (0.02 M HEPES). However, a $\zeta = -15.3$ mV was reported in Ref. 29 (in the less stable region), which may be due to the choice of $R_{\rm H}$ used in the experiment as we found that it affects $\zeta$ significantly. For example, in 0.01 M NaCl the $\zeta$ potentials found at two selected hydroynamic radii, $R_4 = 85$ Å and $R_3 = 64$ Å, are rather different with values, $\zeta = -2.4$ mV, and $\zeta = -11.0$ mV, respectively.

## 3.2 Wrapping effect of PAH on cit-AuNP

*Conformation of cationic polyelectrolyte PAH.* The PAH-AuNP models are built using a steering force that drags a PAH chain on the cit-AuNP surface;[15,32] see Fig. S8 in SI. The attractive interactions between the citrates on the surface and the charged amines of the PAH lead to the spontaneous wrapping by the chains around the AuNPs. Once wrapped, more than 10 ns $NVT$ simulation time is applied to relax the structure. The radius of gyration $R_{\rm g}$ of PAH at different salt concentrations, is available in Figure S9 in SI, and indicates its convergence in the final 10 ns relaxing simulation. Several representative equilibrium structures are also available there. The PAH chains exhibit a larger $R_{\rm g}$ and a better AuNP surface coverage at low salt concentrations as shown in Fig. 4a. For example, the PAH uniformly wraps the cit-AuNP in the 0 M NaCl model, and the $R_{\rm g}$ of PAH is the largest at that molarity. Notably, these structures are similar to the PAH-AuNP wrapped structures reported in Ref. 32 in 0 M and 0.001 M NaCl solutions. At high salt concentration, the PAH chain conformation collapses on the cit-AuNP surface and the $R_{\rm g}$ of PAH decreases (Fig. 4a). This is stabilized by the incorporation of counterions within the condensing chains. In 0.1 M and 0.2 M NaCl, we also find that the PAH coverage is asymmetric as it collapses over the surface of the AuNP giving rise to fairly large $R_{\rm g}$s. These coverages are fairly thin as the positions of the PAH ends shown in Fig. 4b indicate that they reach out only as far as $r \approx 40$ Å, which is not much larger than the observed $R_{\rm g}$s.

*Ion radial distributions near the PAH-AuNP.* The $Na^+$ and $Cl^-$ number densities near PAH-AuNP are calculated using the same method as for their determination near cit-AuNP.

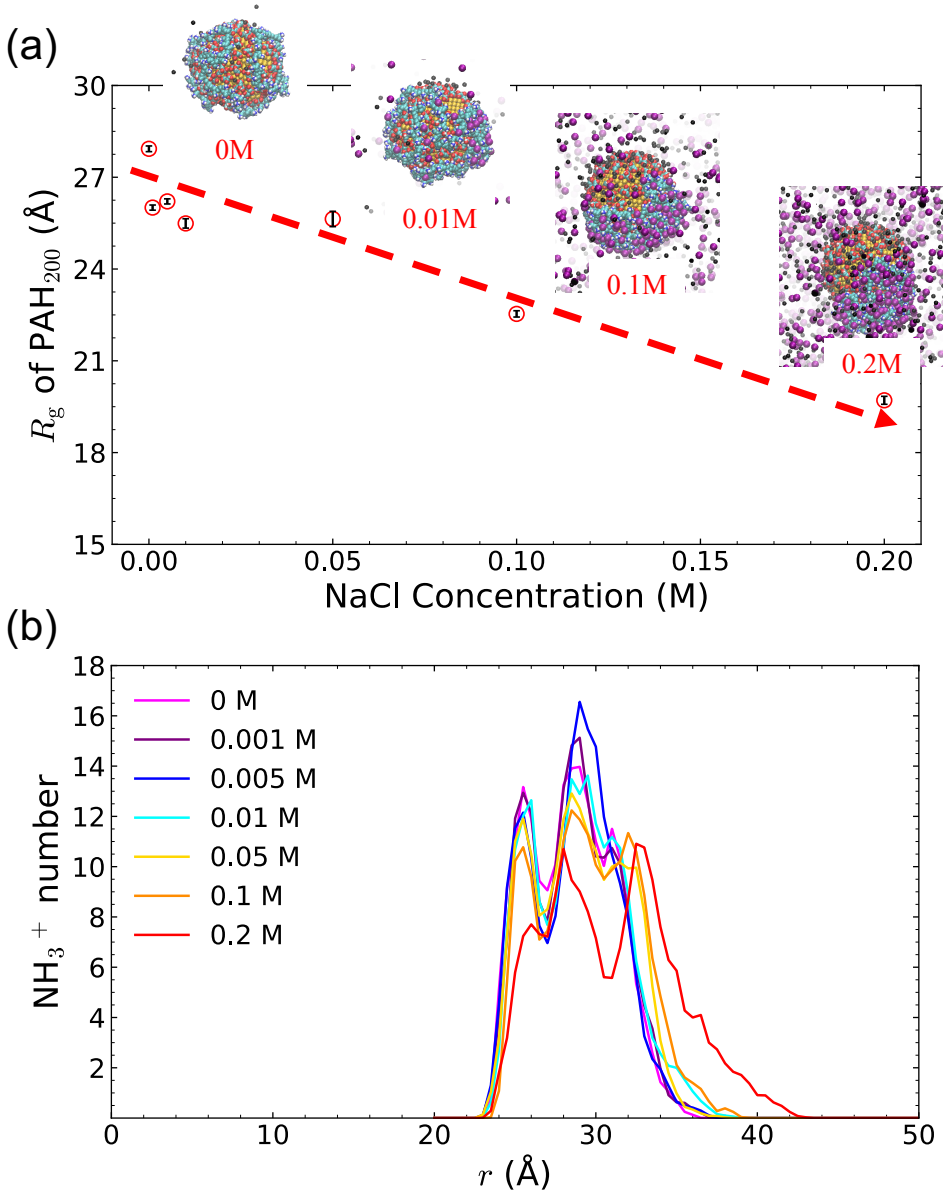


Figure 4: (a) The average radius of gyration $R_g$ of $PAH_{200}$ within PAH-AuNPs at varying NaCl concentration. Representative conformations of the nanoparticles and their salt environment at selected concentrations are also shown to provide a visualization of the arrangement of the PAHs. (b) The number distribution of $NH_3^+$ at the end of the $PAH_{200}$ chains around the nanoparticle, for different salt concentrations.

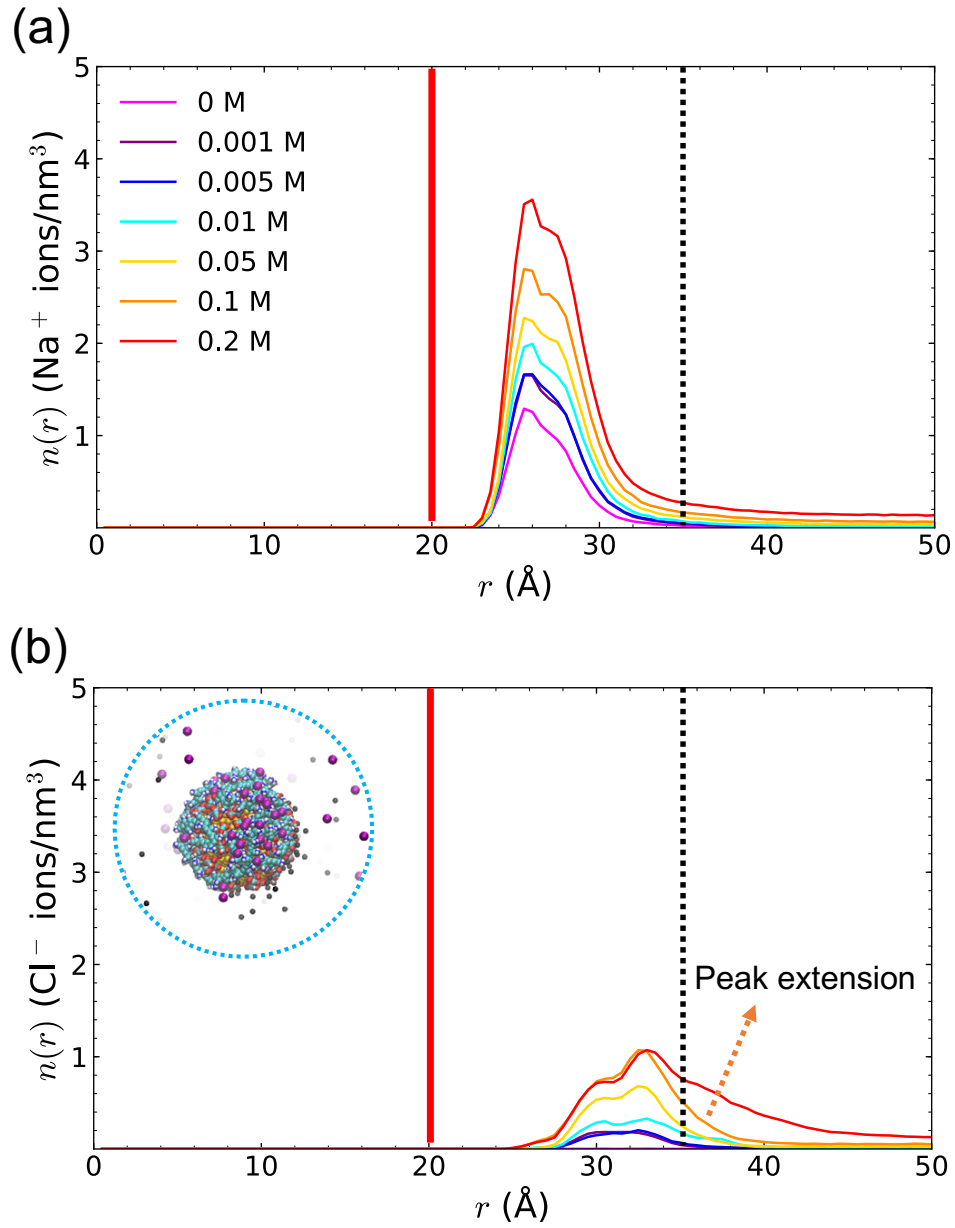


Figure 5: The number density radial distribution of $Na^+$ and $Cl^-$ for the PAH-AuNP model at different NaCl concentrations in (a) and (b), respectively, labeled according to the legend in panel a. The solid line at 20 Å indicates the AuNP surface and the black dotted line at 35 Å indicates the Stern layer position identified earlier for the bare cit-AuNP in Fig. 2. The peak position in $Na^+$ number densities from 20-35 Å shown in panel a coincides with that of cit-AuNP. The $Cl^-$ number density distributions in panel b are shifted to the right because the PAH brings in a significant number of $Cl^-$ extending its Stern layer to 40 Å. The ion number densities beyond a 50 Å radius are reported in Fig. S10 in SI.

Figure 5a shows that the $Na^+$ peak position of the PAH-AuNP is the same as that seen in Fig. 2a for cit-AuNP. However, the peak height in Fig. 4 decreases significantly with decreasing salt concentration due to the replacement of $Na^+$ with the positively charged PAH on the surface. Meanwhile, PAH carries $Cl^-$ co-ions inside the ionic shell which increases the Stern layer thickness up to ∼39 Å; see Fig. 5b. The increase in the $Cl^-$ found in the stern layer is induced by the wrapping by PAH on a AuNP, and the peaks in Fig. 5b are in direct correspondence with the PAH monomer positions seen in Fig. 4b. The quantitative effects on the Stern layer thickness for PAH-AuNP at different NaCl concentrations are reported in Table S5 in SI. We found comparable number densities of $Cl^-$ and $Na^+$ —within the same order of magnitude— inside the Stern layer around PAH-AuNPs as indicated by the comparable y-axis ranges reported in both panels of Fig. 5. However, for cit-AuNP, we report in Fig. 2 that the $Cl^-$ density is a few orders of magnitude lower than $Na^+$. Both $Na^+$ and $Cl^-$ are close to the bulk concentrations at $r > 200$ Å (Fig. S10 in SI), which confirms that the box edge at $r = 500$ Å is sufficiently large. Thus the MD simulations reported here provide an atomistic picture of the structure of PAH wrapped cit-AuNP at different salt concentrations. We found that such wrapping induces significant increases in the $Cl^-$ density near the AuNP surface, and increases the Stern layer thickness. As a result, the co-existing $Na^+$ and $Cl^-$ ions in the Stern layer enhances the interaction of PAH-AuNPs with cell membranes.

*$\zeta$-potential and $R_H$ calculations for the PAH-AuNP.* The total net charge $Z(r)$ surrounding the PAH-AuNP is obtained from the ion distribution found in the MD simulations reported in Fig. S11a of the SI. The electric potential $\phi(r)$ of PAH-AuNP is also calculated from $Z(r)$ using Eq. (1) and shown in Fig. 6a, and Fig. S11b in SI. For simplicity, PAH-AuNP is modeled approximately as an uniform sphere with $r = 20$ Å bearing $Q = -70$ $e$ surface charges. The sharp peak seen at 20-40 Å in Fig. 6a (and in Fig. S11 of the SI) is caused by the wrapping by PAH of the AuNP.

To obtain the $\zeta$-potential and $D_{\mathrm{H}}$, we focus on the region after 40 Å as that is generally

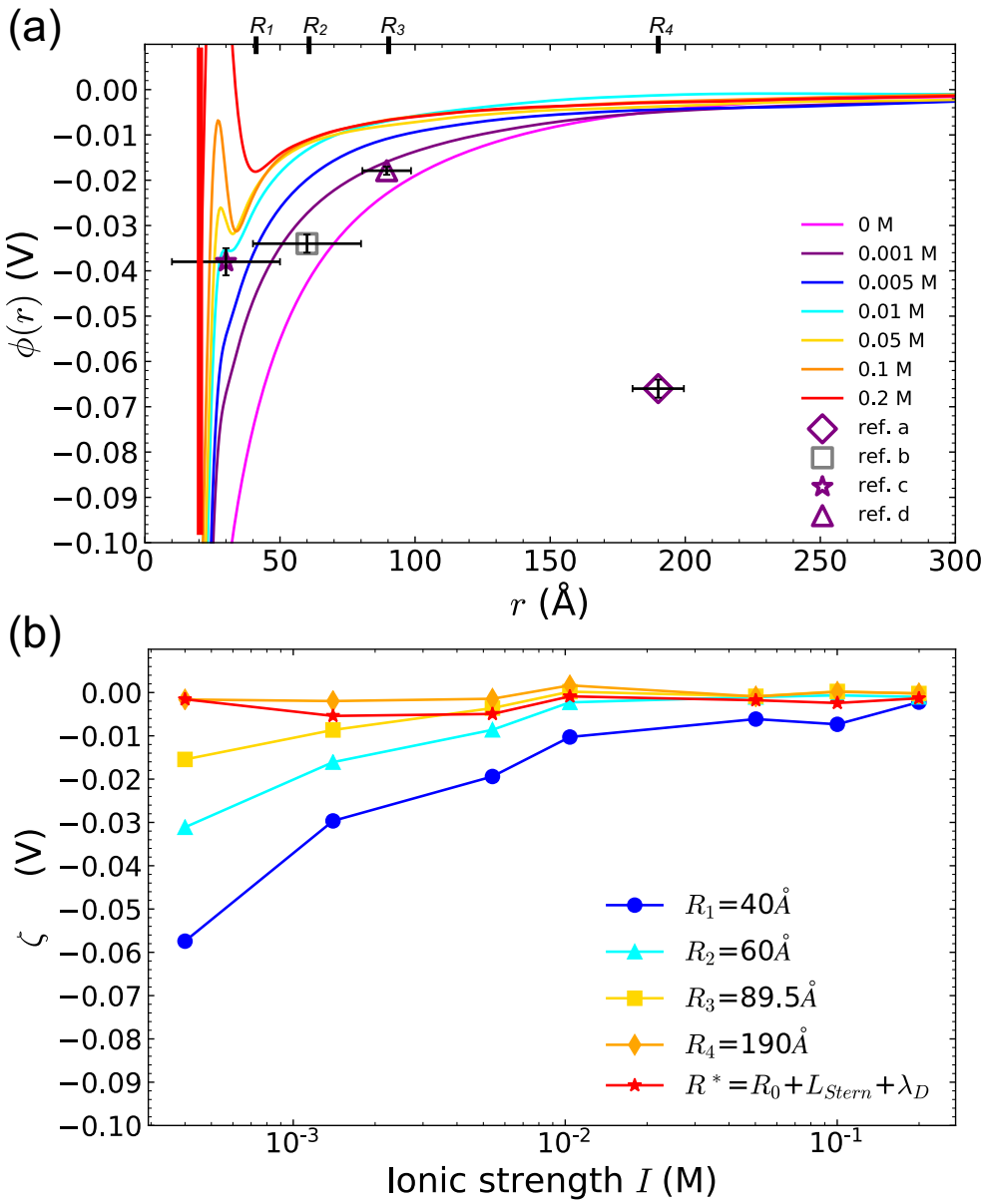


Figure 6: (a) Comparison of the electric potential near PAH-AuNP between those observed in MD simulations at various NaCl concentrations, and those reported in literature. (b) Values of the PAH-AuNP $\zeta$-potential, determined from the MD results in panel a, as a function of the solvent's ionic strength for different estimates of the nanoparticle's hydrodynamic radius $R_{\mathrm{H}}$ whose positions are also noted in panel a. Here, $R_1 = 40$ Å is determined from the MD ion distribution results. Nanoparticles of hydrodyamic radius, $R_2 = 60$ Å, $R_3 = 89.5$ Å and $R_4 = 190$ Å, in 0.02 M HEPES, 0.001 M NaCl, and 0.001 M NaCl were reported in ref. b (viz. Ref. 21), ref. d (viz. Ref. 29), and ref. a (viz. Ref. 20), respectively. Ref. c (viz. Ref. 25) reported nanoparticles with hydrodynamic radius, $R_{\mathrm{H}} = 30$ Å, for a 0.001 M NaCl, but it is not included in this comparision because it is below the Stern layer thickness of 40 Å. All references reported that the $\zeta$-potentials are positive due to the wrapping by multiple PAHs, and the reference $\zeta$-potentials are sign flipped to $-\zeta$ in the figure. As the uncertainty of $D_{\mathrm{H}}$ was not reported in ref. a (viz. Ref. 20), we have included an estimated error bar of 5% throughout.

far enough to find the beginning of the Stern layer and beyond. The Stern layer thickness $L_{\mathrm{Stern}}$ increases from 15 Å to 19 Å in 0.01-0.1 M as reported in Table S5 in SI. The Stern layer remains the same with $L_{\mathrm{Stern}} \approx 15$ Å across a broad domain of 0-0.005 M NaCl concentrations because PAH wraps cit-AuNPs uniformly at low salt concentrations; see schemes in Fig. S9 in SI.

Several radii $R_{\mathrm{H}}$ can be used as the anchor for the $\zeta$-potential calculations illustrated in Fig. 6b. Here, $R_1 = 40$ Å is the position beyond the ion absorption region at which the gradient ion density returns to zero as reported in Fig. S6b in SI. The other distances, $R_2 = 60$ Å, $R_3 = 89.5$ Å and $R_4 = 190$ Å, are the hydrodynamic radii $R_{\mathrm{H}}$ reported in Refs. 21, 29 and 20, respectively. $R_{\mathrm{H}} = 30$ Å reported in Ref. 25 is below the Stern layer, and therefore inappropriate for the calculation of the $\zeta$-potential through the present model. The values of $R^* = R_0 + L_{\mathrm{Stern}} + \lambda_{\mathrm{D}}$ are listed in Table S5 in SI. For PAH-AuNP, we also fit the $Na^+$ distribution with $c \cdot \exp[-e\phi(r)/k_{\mathrm{B}}T]$ and find the slipping layer—that is, when the Debye-Hückel theory is no longer in deviation from the MD simulations[58]—at 40-70 Å (see Fig. S7b in SI). Figure 6 shows that with increasing salt concentration increases, the magnitude of both overall electric potential and $\zeta$-potential decreases. The PAH-AuNP particle is consequently less stable at high salt concentrations.

As recapitulated in Table 1, the experimentally measured $D_{\mathrm{H}}$ for PAH-AuNP vary greatly from 60 Å to 380 Å for similar core size $D_0 \sim 45$ Å in 0.001 M NaCl. We chose $R_{\mathrm{H}} = R_3 = 89.5$ Å for the PAH-AuNP reported in Table 1 in agreement with the value 85 Å found earlier for cit-AuNP. It is a reasonable assumption that after the wrapping by PAH, the $R_{\mathrm{H}}$ slightly increases by 4.5 Å. However, we find $\zeta = -8.6$ mV at $R_3 = 89.5$ Å in 0.001 M NaCl, which is very different from reference values as illustrated in Fig. 6a. Namely, $\zeta = +38$ mV at $R_{\mathrm{H}} = 30$ Å in 0.001 M NaCl, $\zeta = +34$ mV at $R_2 = 60$ Å in 0.02 M HEPES, $\zeta = +17.9$ mV at $R_3 = 89.5$ Å in 0.001 M NaCl and $\zeta = +66$ mV at $R_4 = 190$ Å in 0.001 M NaCl according to Refs. 25, 21, 29 and 20, respectively. One possible origin for the variation between the simulation and experimental results is the assumption in our model that there is only one

PAH chain in the PAH-AuNP model structure. In experiments, the PAH-AuNP assembly has been reported to contain 6-10 PAHs.[25,26] The possible observation of even more PAHs wrapping the AuNP was reported in Ref. 20 for $\zeta = +66$ mV (as also shown in Fig. 6a) which is even larger than that reported by the other references.

The effects of the sequential addition of PAHs to the AuNP can be understood from the behavior of the present model for a single PAH interacting with a cit-AuNP. After a single PAH wraps the nanoparticle, the surface charge changes from $-270$ $e$ to $-70$ $e$, and the $\zeta$-potential changes from $-25.5$ mV cit-AuNP to $-8.6$ mV PAH-AuNP in 0.001 M NaCl, at $R_{\rm H} = 85$ Å and 89.5 Å, respectively. As additional PAHs wrap a nanoparticle, we would then expect the $\zeta$-potential to increase. With enough of them, it is not surprising that they would become positive reported in the experimental $\zeta$-potentials. Table 1 lists the $\zeta$-potentials reported from experiments with values ranging from $-35$ mV Ref. 30 to $+66$ mV Ref. 20. The $-35$ mV is the only reported negative $\zeta$ for PAH-AuNP. Such a big discrepancy may be due to the surface charge of the PAH-AuNP can vary from +200 e to $-200$ e as reported in Refs. 25 and 26 or from AuNPs with few attached PAHs. The confirmation of the surface charge and $\zeta$-potential for the PAH-AuNP with more precision on the degree of PAH attachment in experiment is therefore necessary to resolve this question.

We found that the $\zeta$-potential magnitude drops from $-25.5$, $-2.4$ and $+0.3$ mV to $-8.6$, $+0.2$ and $+0.2$ mV, after one PAH wraps a cit-AuNP in 0.001 M, 0.01 M and 0.1 M NaCl, respectively; see Table 1. This result confirms that PAH-AuNP is less stable than cit-AuNP, and both particles are less stable at high salt concentrations. We also found that the $\phi(r)$ is pushed towards zero after wrapping by PAH; see Figs. 3a and 6a.

*Comparison between cit-AuNP and PAH-AuNP at 0.01 M NaCl.* We focus on this case because it corresponds to a typical salt concentration in the cellular environment. The ionic concentrations for both cit-AuNP and PAH-AuNP converge after $\sim$370 Å as can be seen in Fig. 7a. The $Na^+$ number densities for both colloids have the same shape, except that the peak height at 27 Å drops in PAH-AuNP; see Fig. S12a in SI. However, the $Cl^-$

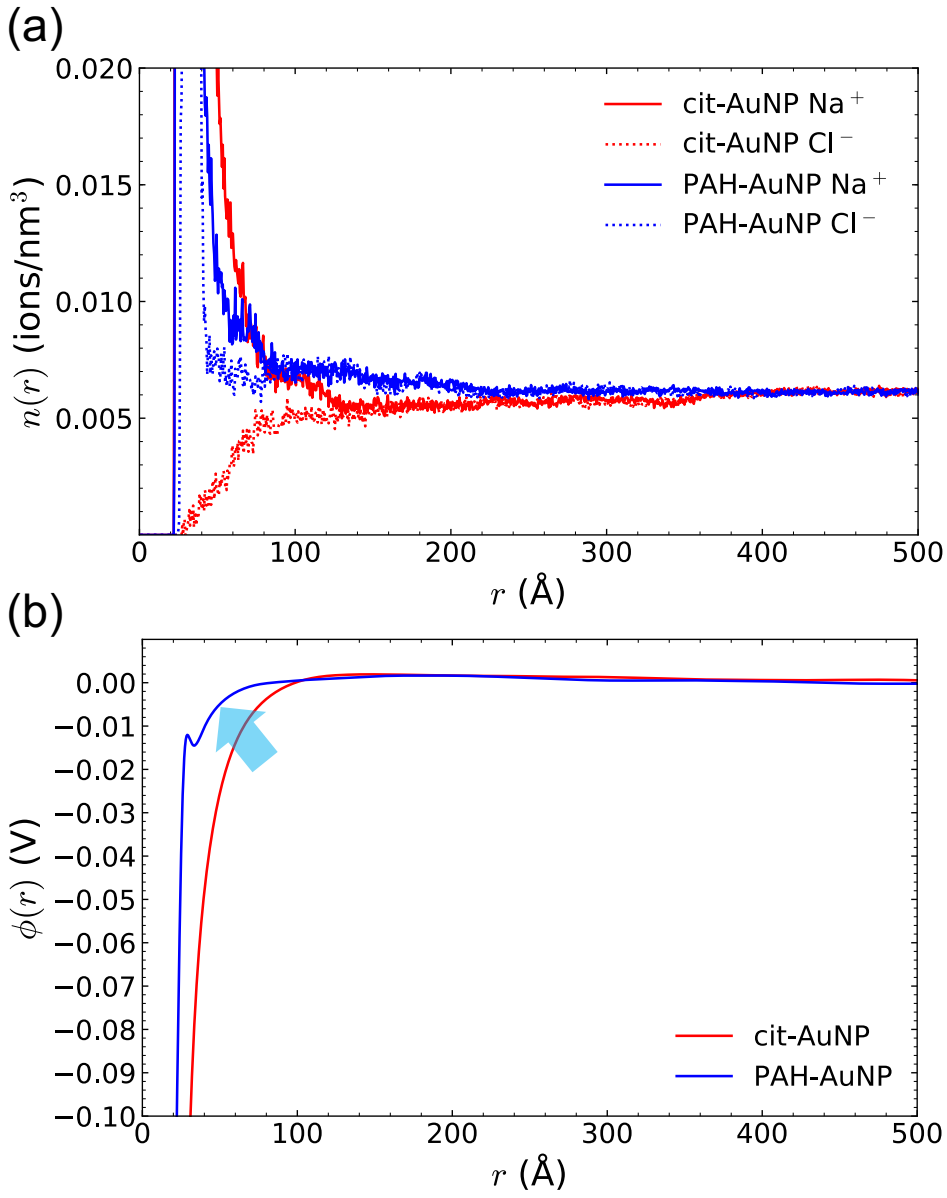


Figure 7: Comparison of observables before and after PAH wrapping on cit-AuNP relative to those from models at 0.01 M NaCl concentration: (a) $Na^+$ and $Cl^-$ number densities near the AuNP surface, as labeled in the figure caption. (b) The magnitude of the electric potential at $r$ <100 Å reduces significantly after PAH wraps a bare cit-AuNP. The arrow highlights the signficant shift in the electric potential of the cit-AuNP caused by the addition of PAH.

number densities are significantly different. Before the PAH wraps cit-AuNP, the $Cl^-$ number density climbs slowly towards the bulk concentration in Fig. 7a. After the wrapping by PAH wrapping, the $Cl^-$ forms a secondary peak at 30-35 Å (see Fig. S12a in SI), and then the $Cl^-$ peak decreases towards the bulk concentration as shown in Fig. 7a. The $Cl^-$ co-ions carried onto the nanoparticle surface by PAH could enhance the interactions of the nanoparticle to biomembranes which could be important to nano-bio applications.[18] Figure S12b in SI shows that before the PAH wraps cit-AuNP, $Z(r)$ starts from $-270$ $e$ at 20 Å and it is neutralized to zero by ions at $r \sim 120$ Å. After PAH wraps a PAH-AuNP, $Z(r)$ starts from $-70$ $e$ at 20 Å and it is immediately neutralized to zero by ions at $r \sim 60$ Å. As a result, the electric potential $\phi(r)$ of PAH-AuNP shifts towards zero dramatically after the wrapping by PAH, making the PAH-AuNP less stable than cit-AuNP; see Fig. 7b. For example, at $r = 50$ Å, we found that after wrapping by PAH, $|\phi(r)|$ reduces from 25.5 to 5.0 mV. Thus, the comparison between the 0.01 M NaCl AuNP models suggests that wrapping by PAH leads to PAH-AuNPs with increase reactivity and stability.

## 3.3 PBE approxiation and DLVO theory

*Electric potential calculation.* The Stern layer thicknesses ($L_{\text{Stern}}$) of cit-AuNP and PAH-AuNP are estimated from the ion concentrations and charge distributions (available in Fig. S13 in SI). The effective colloid radius ($a_i = 20$ Å$+L_{\text{Stern}}$) can then be determined as the sum of the core radius (20 Å) and the Stern layer thickness. We found that cit-AuNPs have an approximately constant $L_{\text{Stern}} = 15$ Å, and the PAH-AuNPs have $L_{\text{Stern}}$ values range from 15-28 Å. The explicit values for both nanoparticles under varying conditions are avaialble in Table S5 in SI. The surface charges $Z(a_i)$ obtained at the Stern layer are also available in Figs. S13a and S13d and Table S4 in SI. The results from the PBE calculations—presented in Fig. 8—exhibit the expected trend that $\phi(r)$ shifts to zero with increasing salt concentration or due to the wrapping by PAH. The results from the DLVO calculations—presented in Fig. 8 and detailed in Table S4 in SI— exhibit more distinguishable differences due to changes in salt

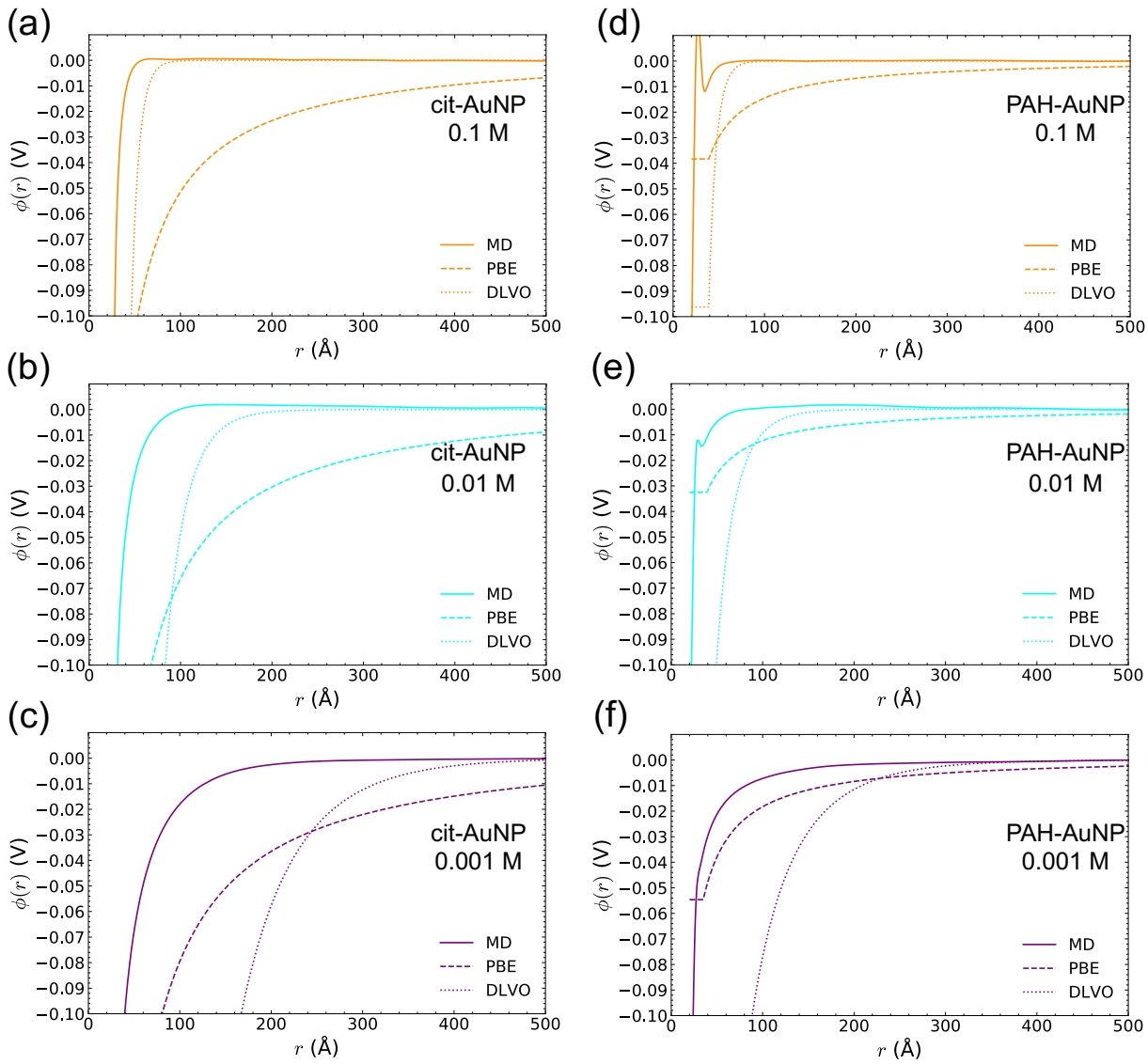


Figure 8: Comparison of electric potential curves calculated from three different methods, viz. MD, PBE and DLVO: cit-AuNP in 0.1 M (a), 0.01 M (b) and 0.001 M NaCl (c), and PAH-AuNP in 0.1 M (d), 0.01 M (e) and 0.001 M NaCl (f). Solid, dashed and dotted lines represent results obtained with MD, PBE and DLVO methods, respectively.

concentration; see also Figs. S13c and S13f in SI. This is not surprising because the Debye length ($\lambda_D$) plays a key role in DLVO theory leading to dramatic variations in $\lambda_D$ with salt concentration. Thus both PBE and DLVO methods lead to a shift of $\phi(r)$ to zero—that is, reduced stability—with increasing salt concentration.

*Comparison between theory and MD results.* The MD, PBE and DLVO results for $\phi(r)$ at different salt concentrations (0.001 M, 0.01 M and 0.1 M NaCl) for both cit-AuNP and PAH-AuNP are compared in Fig. 8. We found that PBE overestimates $\phi(r)$ at all salt concentrations for both cit-AuNP and PAH-AuNP. Resetting $\phi(r) = 0$ at 800 Å in the MD simulations does not close the gap to the PBE results. The main reason for the discrepency between PBE and MD results is that the naive PBE approximation assumes ions are independent and that the ion-ion interaction is negligible. Thus the results in Fig. 8 indicate that at low salt concentrations, the PBE approximation, though far from exact, is in better agreement with MD than the DLVO theory. The PBE approximation is also a better match to MD at low surface charges as indicated in Fig. 8.

Meanwhile, we see in Fig. 8 that the large $r$ limits of the electric potential predicted by DLVO matches those observed in MD at all of the salt concentrations we observed. At high NaCl concentrations (such as 0.1 M), the agreement is very good except for a small mismatch in the onset of the potential. That mismatch grows with decreasing salt concentration. The derivation of DLVO Eq. (14) starts from the assumption in Debye-Hückel theory that $\kappa a >> 1$, where $\kappa = 1/\lambda_D$.[51,59,60] This is satisfied for strong electrolytes and small $\lambda_D$, which is at sufficiently large concentrations, see Eq. (13). For small nanoparticles, the strong condition, $\kappa a >> 1$, can be easily violated. In our models, the values of $a_i$ and $\lambda_D$ are reported in Table S4 in SI, resulting in $\kappa a = 3.65$, 1.16 and 0.40 for cit-AuNP at 0.1, 0.01 and 0.001 M NaCl, respectively. Meanwhile, $\kappa a = 4.02$, 1.29 and 0.42 for PAH-AuNP at 0.1, 0.01 and 0.001 M NaCl, respectively. The cases with the largest $\kappa a$ take place at high concentration (0.1 M) and give rise to the best agreement because their values are only moderately larger than 1. Thereafter, the decreasing agreement in the onset of the electric

potential with respect to salt concentration trends with decreasing $\kappa a$. In summary, the naive PBE approximation has limited application at low salt concentration and at low surface charge density. The DLVO approach appears to be the best choice for modeling colloid-colloid interactions when the AuNPs are relatively large and $\kappa a >> 1$ is easily satisfied. In such cases, Eq. (14) provides a simple framework for its implementation, and we have found that it is sufficiently accurate to reveal the system properties.

# 4 Conclusions

In this work, we use MD simulations to reveal the electric potential near cit-AuNPs and PAH-AuNPs, at various NaCl concentrations, 0, 0.001, 0.005, 0.01, 0.05, 0.1, 0.2 M. The cit-AuNP model is a 4 nm diameter AuNP capped with 90 $\text{Citrate}^{3-}$ molecules, and the PAH-AuNP model is one PAH wrapping the cit-AuNP. The radial distributions of the ionic number density—viz, their concentraion—near the surface of the nanoparticles were histogrammed over the reported MD simulations. The net charge distribution ($Z(r)$) is calculated using the ionic number density. In turn, the electric potential ($\phi(r)$) was calculated using Gauss's law. The features of the MD-generated $\phi(r)$ for both cit-AuNP and PAH-AuNP are compared to the experimentally measured $\zeta$-potentials and $R_{\text{H}}$ in literature. We find that the magnitude of the $\zeta$-potential decreases with increasing NaCl concentration. Perhaps not surprisingly, it decreases when it is measured at increasing $R_{\text{H}}$.

Specifically, we found consensus estimates of the hydrodynamic radii for cit-AuNP and PAH-AuNP as $R_{\text{H}} = 85$ Å and $R_{\text{H}} = 89.5$ Å, respectively. The $\zeta$-potentials for cit-AuNP at its hydrodynamic radius are $-25.5$, $-2.4$ and $+0.3$ mV in 0.001 M, 0.01 M and 0.1 M NaCl solutions, respectively. The value for cit-AuNP in 0.001 M NaCl is comparable to many experimental results cited herein, and is consistent with the observation that cit-AuNP is stable at low salt concentrations (0.001 M NaCl). The addition of PAH shifts the $\zeta$-potentials for PAH-AuNP to $-8.6$, $+0.2$ and $+0.2$ mV in 0.001 M, 0.01 M and 0.1 M NaCl, respectively.

We thus find that the addition with just one PAH chain, the $\zeta$-potential magnitude reduces significantly, in 0.001 M NaCl changing from cit-AuNP stable ($|\zeta| \sim 30$ mV) to PAH-AuNP unstable ($|\zeta| < 10$ mV). At high salt concentrations, both cit-AuNP and PAH-AuNP are unstable, again in agreement with prior experimental reports. We also observe that a large number of $Cl^-$ ions are brought into the Stern layer upon the addition of PAH. These $Cl^-$ ions form a secondary ion peak at 30-35 Å coincident with the extension of the PAH chains to about 40 Å. Our work thus confirms the fact that after the addition of PAH, the stability of the AuNP colloid is significantly reduced. This bears on nano-bio interactions in cell membranes because AuNPs wrapped by PAHs forming its corona evidently become more reactive.

We also report a comparative analysis of our MD results for $\phi(r)$ to those from the classic PBE approximation and the well-known DLVO theory. We found that the PBE approximation can overestimate $\phi(r)$ because the ion-ion interaction is not considered in the PBE theory. The PBE result is in better agreement with the MD results at low salt concentration and low surface charge density, which occurs for example when PAH-AuNP is in 0.001 M NaCl solution. Meanwhile, our results confirm that DLVO theory is accurate when the nanoparticle size is much larger than the corresponding Debye length. Thus the advantages of this simplified theory widely used to describe large colloidal particle interactions are also relevant for nanoparticles, albeit it under the condition that they are large in comparison with the Debye length.

# Acknowledgments

We thank Catharine J. Murphy for a careful reading of this manuscript. This work was supported by the National Science Foundation under Grant No. CHE-2001611, the NSF Center for Sustainable Nanotechnology (CSN). The CSN is part of the NSF Centers for Chemical Innovation Program. The computing resources necessary for this research were

provided in part by the National Science Foundation through XSEDE resources under Grant No. CTS090079, and the Advanced Research Computing at Hopkins (ARCH) facilities supported by the NSF MRI Grant (OAC-1920103).

## Supplementary Information

The Supporting Material (SM) includes the following content: detailed information about simulation methods and results.

## Data Availability

The data that support the findings of this study are available from the corresponding author upon reasonable request.

## References

## References

(1) Saha, K.; Agasti, S. S.; Kim, C.; Li, X.; Rotello, V. M. Gold Nanoparticles in Chemical and Biological Sensing. *Chem. Rev.* **2012**, *112*, 2739.

(2) Dreaden, E. C.; Alkilany, A. M.; Huang, X.; Murphy, C. J.; El-Sayed, M. A. The golden age: Gold nanoparticles for biomedicine. *Chem. Soc. Rev.* **2012**, *41*, 2740–2779.

(3) Yang, X.; Yang, M.; Pang, B.; Vara, M.; Xia, Y. Gold nanomaterials at work in biomedicine. *Chem. Rev.* **2015**, *115*, 10410–10488.

(4) Bathe, M.; Hernandez, R.; Komiyama, T.; Machiraju, R.; Neogi, S. Autonomous computing materals. *ACS Nano* **2021**, *15*, 3586–3592.

(5) Wei, X.; Zhao, Y.; Zhuang, Y.; Hernandez, R. Engineered nanoparticle network models for autonomous computing. *J. Chem. Phys.* **2021**, *154*, 214702.

(6) Turkevich, J.; Stevenson, P. C.; Hillier, J. A study of the nucleation and growth processes in the synthesis of colloidal gold. *Discuss. Faraday Soc.* **1951**, *11*, 55–75.

(7) Kimling, J.; Maier, M.; Okenve, B.; Kotaidis, V.; Ballot, H.; Plech, A. Turkevich method for gold nanoparticle synthesis revisited. *J. Phys. Chem. B* **2006**, *110*, 15700–15707.

(8) Chen, F.; Li, X.; Hihath, J.; Huang, Z.; Tao, N. Effect of anchoring groups on single-molecule conductance: comparative study of thiol-, amine-, and carboxylic-acid-terminated molecules. *J. Am. Chem. Soc.* **2006**, *128*, 15874–15881.

(9) Park, J.-W.; Shumaker-Parry, J. S. Structural study of citrate layers on gold nanoparticles: Role of intermolecular interactions in stabilizing nanoparticles. *J. Am. Chem. Soc.* **2014**, *136*, 1907–1921.

(10) Park, J.-W.; Shumaker-Parry, J. S. Strong resistance of citrate anions on metal nanoparticles to desorption under thiol functionalization. *ACS Nano* **2015**, *9*, 1665–1682.

(11) Al-Johani, H. et al. The structure and binding mode of citrate in the stabilization of gold nanoparticles. *Nat. Chem.* **2017**, *9*, 890–895.

(12) Provorse, M. R.; Aikens, C. M. Binding of carboxylates to gold nanoparticles: A theoretical study of the adsorption of formate on Au20. *Comput. Theor. Chem.* **2012**, *987*, 16–21.

(13) Wright, L. B.; Rodger, P. M.; Walsh, T. R. Structure and properties of citrate overlayers adsorbed at the aqueous Au(111) interface. *Langmuir* **2014**, *30*, 15171–15180.

(14) Monti, S.; Barcaro, G.; Sementa, L.; Carravetta, V.; Ågren, H. Characterization of the

adsorption dynamics of trisodium citrate on gold in water solution. *RSC Adv.* **2017**, *7*, 49655–49663.

(15) Chong, G.; Laudadio, E. D.; Wu, M.; Murphy, C. J.; Hamers, R. J.; Hernandez, R. Density, structure, and stability of citrate$^{3-}$ and $H_2$citrate$^{-}$ on bare and coated gold nanoparticles. *J. Phys. Chem. C* **2018**, *122*, 28393–28404.

(16) Maurer-Jones, M. A.; Gunsolus, I. L.; Murphy, C. J.; Haynes, C. L. Toxicity of engineered nanoparticles in the environment. *Anal. Chem.* **2013**, *85*, 3036–3049.

(17) Feng, Z. V.; Gunsolus, I. L.; Qiu, T. A.; Hurley, K. R.; Nyberg, L. H.; Frew, H.; Johnson, K. P.; Vartanian, A. M.; Jacob, L. M.; Lohse, S. E.; Torelli, M. D.; Hamers, R. J.; Murphy, C. J.; Haynes, C. L. Impacts of gold nanoparticle charge and ligand type on surface binding and toxicity to Gram-negative and Gram-positive bacteria. *Chem. Sci.* **2015**, *6*, 5186–5196.

(18) Murphy, C. J.; Vartanian, A. M.; Geiger, F. M.; Hamers, R. J.; Pedersen, J.; Cui, Q.; Haynes, C. L.; Carlson, E. E.; Hernandez, R.; Klaper, R. D.; Orr, G.; Rosenzweig, Z. Biological responses to engineered nanomaterials: Needs for the next decade. *ACS Cent. Sci.* **2015**, *1*, 117.

(19) Cui, Q.; Hernandez, R.; Mason, S. E.; Frauenheim, T.; Pedersen, J. A.; Geiger, F. Mini-review. Sustainable nanotechnology: Opportunities and challenges for theoretical/computational studies. *J. Phys. Chem. B* **2016**, *120*, 7297–7306.

(20) Qiu, T. A.; Torelli, M. D.; Vartanian, A. M.; Rackstraw, N. B.; Buchman, J. T.; Jacob, L. M.; Murphy, C. J.; Hamers, R. J.; Haynes, C. L. Quantification of free polyelectrolytes present in colloidal suspension, revealing a source of toxic responses for polyelectrolyte-wrapped gold nanoparticles. *Anal. Chem.* **2017**, *89*, 1823–1830.

(21) Buchman, J. T.; Rahnamoun, A.; Landy, K. M.; Zhang, X.; Vartanian, A. M.; Jacob, L. M.; Murphy, C. J.; Hernandez, R.; Haynes, C. L. Using an environmentally-

relevant panel of Gram-negative bacteria to assess the toxicity of polyelectrolyte-wrapped gold nanoparticles. *Environ. Sci. Nano* **2018**, *5*, 279–288.

(22) Gole, A.; Murphy, C. J. Polyelectrolyte-coated sold nanorods: Synthesis, characterization and immobilization. *Chem. Mater.* **2005**, *17*, 1325–1330.

(23) Lohse, S. E.; Eller, J. R.; Sivapalan, S. T.; Plews, M. R.; Murphy, C. J. A simple millifluidic genchtop reactor system for the high-throughput synthesis and functionalization of gold nanoparticles with different sizes and shapes. *ACS Nano* **2013**, *7*, 4135–4150.

(24) Lin, W.; Insley, T.; Tuttle, M. D.; Zhu, L. Y.; Berthold, D. A.; Král, P.; Rienstra, C. M.; Murphy, C. J. Control of protein orientation on gold nanoparticles. *J. Phys. Chem. C* **2015**, *119*, 21035–21043.

(25) Troiano, J. M. et al. Direct probes of 4 nm diameter gold panoparticles interacting with supported lipid bilayers. *J. Phys. Chem. C* **2015**, *119*, 534–546.

(26) Troiano, J. M.; Kuech, T. R.; Vartanian, A. M.; Torelli, M. D.; Sen, A.; Jacob, L. M.; Hamers, R. J.; Murphy, C. J.; Pedersen, J. A.; Geiger, F. M. On electronic and charge interference in second harmonic generation responses from gold metal nanoparticles at supported lipid bilayers. *J. Phys. Chem. C* **2016**, *120*, 20659–20667.

(27) Bhattacharjee, S. DLS and zeta potential – What they are and what they are not? *J. Control. Release* **2016**, *235*, 337–351.

(28) Rostek, A.; Mahl, D.; Epple, M. Chemical composition of surface-functionalized gold nanoparticles. *J. Nanopart. Res.* **2011**, *13*, 4809–4814.

(29) Dominguez, G. A.; Lohse, S. E.; Torelli, M. D.; Murphy, C. J.; Hamers, R. J.; Orr, G.; Klaper, R. D. Effects of charge and surface ligand properties of nanoparticles on oxidative stress and gene expression within the gut of Daphnia magna. *Aquat. Toxicol.* **2015**, *162*, 1–9.

(30) Han, L.; Zhao, J.; Zhang, X.; Cao, W.; Hu, X.; Zou, G.; Duan, X.; Liang, X.-J. Enhanced siRNA delivery and silencing gold–chitosan nanosystem with surface charge-reversal polymer assembly and good biocompatibility. *ACS Nano* **2012**, *6*, 7340–7351.

(31) Clark, A. E.; Adams, H.; Hernandez, R.; Krylov, A. I.; Niklasson, A. M. N.; Sarupria, S.; Wang, Y.; Wild, S. M.; Yang, Q. The middle science: Traversing scale in complex many-body systems. *ACS Cent. Sci.* **2021**, *7*, 1271.

(32) Chong, G.; Hernandez, R. Adsorption dynamics and structure of polycations on citrate-coated gold nanoparticles. *J. Phys. Chem. C* **2018**, *122*, 19962–19969.

(33) Rostek, A.; Mahl, D.; Epple, M. Chemical composition of surface-functionalized gold nanoparticles. *J. Nanopart. Res.* **2011**, *13*, 4809–4814.

(34) Dominguez, G. A.; Lohse, S. E.; Torelli, M. D.; Murphy, C. J.; Hamers, R. J.; Orr, G.; Klaper, R. D. Effects of charge and surface ligand properties of nanoparticles on oxidative stress and gene expression within the gut of *Daphnia magna*. *Aquat. Toxicol.* **2015**, *162*, 1–9.

(35) Brancolini, G.; Corazza, A.; Vuano, M.; Fogolari, F.; Mimmi, M. C.; Bellotti, V.; Stoppini, M.; Corni, S.; Esposito, G. Probing the influence of citrate-capped gold nanoparticles on an amyloidogenic protein. *ACS Nano* **2015**, *9*, 2600–2613.

(36) Plimpton, S. J. Fast parallel algorithms for short-range molecular dynamics. *J. Comput. Phys.* **1995**, *117*, 1–19, https://www.lammps.org.

(37) Heinz, H.; Vaia, R. A.; Farmer, B. L.; Naik, R. R. Accurate simulation of surfaces and interfaces of face-centered cubic metals using 12-6 and 9-6 Lennard-Jones potentials. *J. Phys. Chem. C* **2008**, *112*, 17281–17290.

(38) Ponder, J. W.; Richards, F. M. An efficient newton-like method for molecular mechanics energy minimization of large molecules. *J. Comput. Chem.* **1987**, *8*, 1016–1024.

(39) Rackers, J. A.; Wang, Z.; Lu, C.; Laury, M. L.; Lagardere, L.; Schnieders, M. J.; Piquemal, J.-P.; Ren, P.; Ponder, J. W. Tinker 8: Software tools for molecular design. *J. Chem. Theory Comput.* **2018**, *14*, 5273–5289, https://dasher.wustl.edu/tinker/.

(40) Jorgensen, W. L.; Maxwell, D. S.; Tirado-Rives, J. Development and testing of the OPLS all-atom force field on conformational energetics and properties of organic liquids. *J. Am. Chem. Soc.* **1996**, *118*, 11225–11236.

(41) Wei, X.; Zhao, Y.; Zhuang, Y.; Hernandez, R. Building blocks for autonomous computing materials: Dimers, trimers and tetramers,. *J. Chem. Phys.* **2021**, *154*, 154704.

(42) Ahn, Y.; Saha, J. K.; Schatz, G. C.; Jang, J. Molecular dynamics study of the formation of a self-assembled monolayer on gold. *J. Phys. Chem. C* **2011**, *115*, 10668–10674.

(43) Singh, U. C.; Kollman, P. A. An approach to computing electrostatic charges for molecules. *J. Comput. Chem.* **1984**, *5*, 129–145.

(44) Kolafa, J.; Perram, J. W. Cutoff errors in the Ewald summation formulae for point charge systems. *Mol. Sim.* **1992**, *9*, 351–368.

(45) Fennell, C. J.; Gezelter, J. D. Is the Ewald summation still necessary? Pairwise alternatives to the accepted standard for long-range electrostatics. *J. Chem. Phys.* **2006**, *124*, 234104.

(46) Heikkilä, E.; Gurtovenko, A. A.; Martinez-Seara, H.; Häkkinen, H.; Vattulainen, I.; Akola, J. Atomistic simulations of functional $Au_{144}(SR)_{60}$ gold nanoparticles in aqueous environmene. *J. Phys. Chem. C* **2012**, *116*, 9805–9815.

(47) López-García, J. J.; Horno, J.; Grosse, C. Equilibrium electric double layer of charged spherical colloidal particles: Effect of different distances of minimum ion approach to the particle surface. *J. Phys. Chem. B* **2010**, *114*, 7548–7556.

(48) López-García, J. J.; Horno, J.; Grosse, C. Poisson–Boltzmann description of the electrical double layer including ion size effects. *Langmuir* **2011**, *27*, 13970–13974.

(49) Kilic, M. S.; Bazant, M. Z.; Ajdari, A. Steric effects in the dynamics of electrolytes at large applied voltages. I. Double-layer charging. *Phys. Rev. E* **2007**, *75*, 021502.

(50) Kilic, M. S.; Bazant, M. Z.; Ajdari, A. Steric effects in the dynamics of electrolytes at large applied voltages. II. Modified Poisson-Nernst-Planck equations. *Phys. Rev. E* **2007**, *75*, 021503.

(51) Verwey, E. J. W.; Overbeek, J. T. G. Theory of the stability of lyophobic colloids. *J. Colloid Sci.* **1955**, *10*, 224–225.

(52) Belloni, L. Electrostatic interactions in colloidal solutions: Comparison between primitive and one-component models. *J. Chem. Phys.* **1986**, *85*, 519–526.

(53) Vlachy, V. Ionic effects beyond Poisson-Boltzmann theory. *Annu. Rev. Phys. Chem.* **1999**, *50*, 145–165.

(54) Belloni, L. Colloidal interactions. *J. Phys.: Condens. Matter* **2000**, *12*, R549–R587.

(55) Guerrero-García, G. I.; González-Mozuelos, P.; de la Cruz, M. O. Large counterions boost the solubility and renormalized charge of suspended nanoparticles. *ACS Nano* **2013**, *7*, 9714–9723.

(56) Boon, N.; Guerrero-García, G. I.; van Roij, R.; de la Cruz, M. O. Effective charges and virial pressure of concentrated macroion solutions. *Proc. Natl. Acad. Sci. U.S.A.* **2015**, *112*, 9242–9246.

(57) Boulos, S. P.; Davis, T. A.; Yang, J. A.; Lohse, S. E.; Alkilany, A. M.; Holland, L. A.; Murphy, C. J. Nanoparticle–protein interactions: A thermodynamic and kinetic study of the adsorption of bovine serum albumin to gold nanoparticle surfaces. *Langmuir* **2013**, *29*, 14984–14996.

(58) Liang, D.; Dahal, U.; Zhang, Y. K.; Lochbaum, C.; Ray, D.; Hamers, R. J.; Pedersen, J. A.; Cui, Q. Interfacial water and ion distribution determine $\zeta$ potential and binding affinity of nanoparticles to biomolecules. *Nanoscale* **2020**, *12*, 18106–18123.

(59) Delgado, Á. V.; González-Caballero, F.; Hunter, R. J.; Koopal, L. K.; Lyklema, J. Measurement and interpretation of electrokinetic phenomena. *J. Colloid Interface Sci.* **2007**, *309*, 194–224.

(60) Hotze, E. M.; Phenrat, T.; Lowry, G. V. Nanoparticle aggregation: Challenges to understanding transport and reactivity in the environment. *J. Environ. Qual.* **2010**, *39*, 1909–1924.

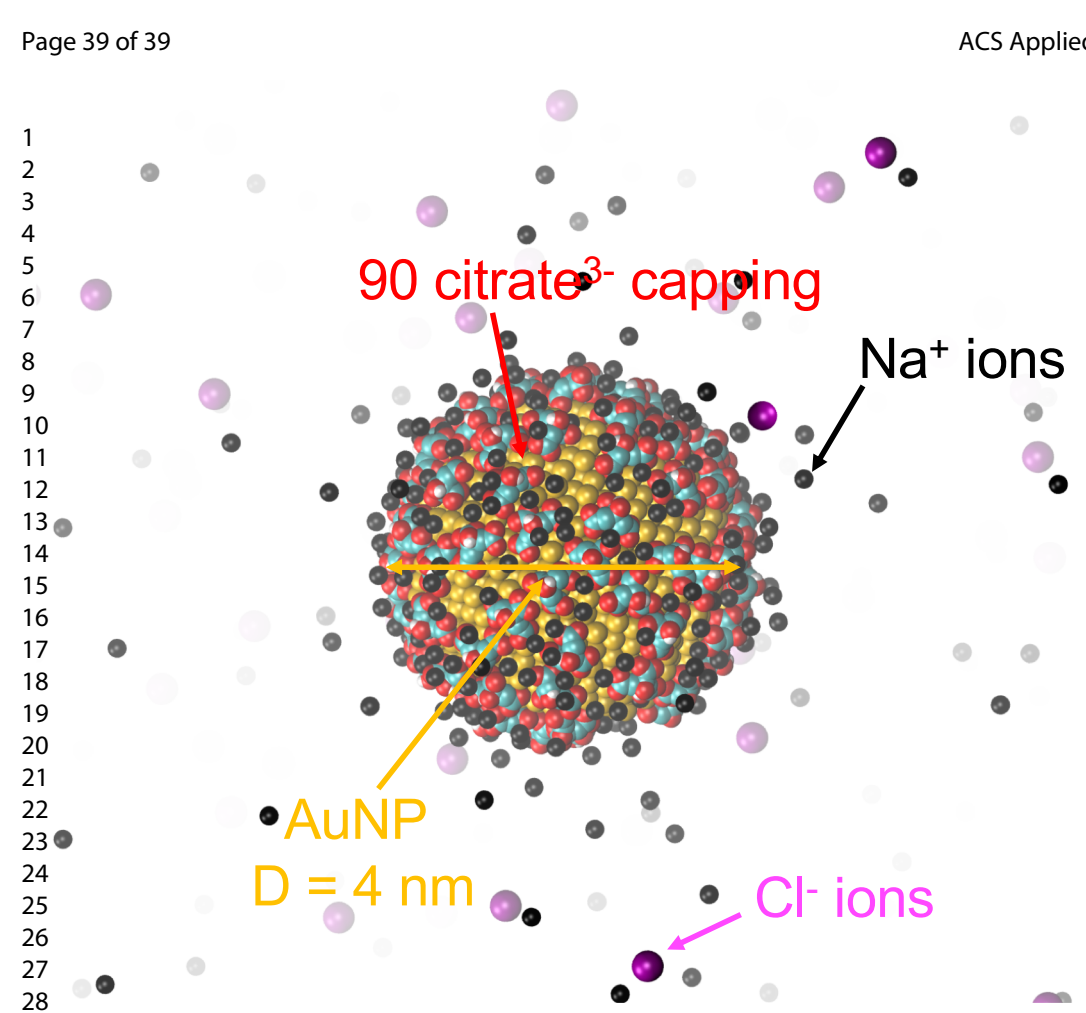
90 citrate3- capping
Na+ ions
AuNP
D = 4 nm
Cl- ions

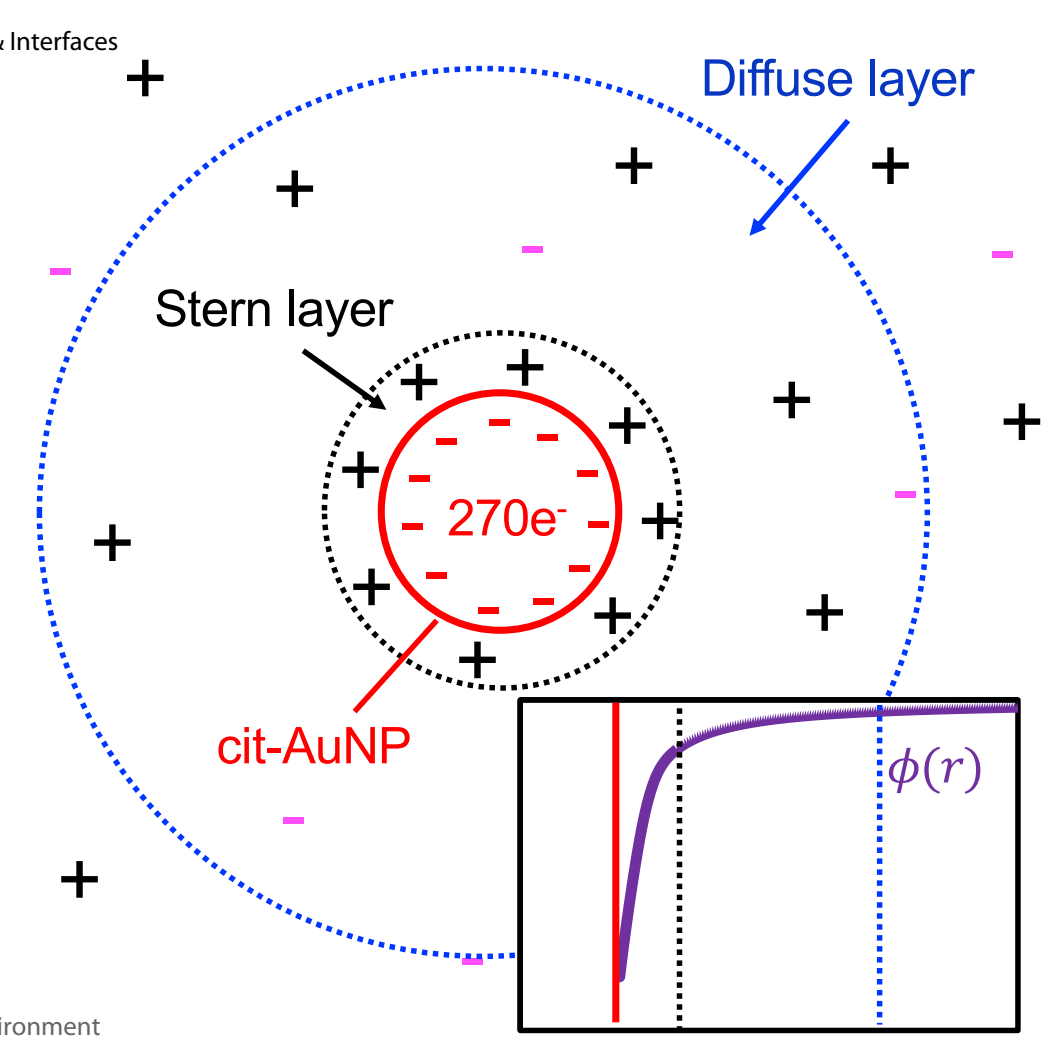
Diffuse layer
Stern layer
270e-
cit-AuNP
$\phi(r)$